4

Mass Dependence of Equilibrium Oxygen Isotope Fractionation in Carbonate, Nitrate, Oxide, Perchlorate, Phosphate, Silicate, and Sulfate Minerals

Edwin A. Schauble and Edward D. Young

Department of Earth, Planetary, and Space Sciences
UCLA
Los Angeles, CA 90095-1567
USA

schauble@g.ucla.edu
eyoung@epss.ucla.edu

INTRODUCTION

Variation in both $^{18}O/^{16}O$ and $^{17}O/^{16}O$ ratios in natural materials can now be measured with unprecedented precision, with a broad range of potential geochemical applications. In this chapter, equilibrium $^{18}O/^{16}O$ and $^{17}O/^{16}O$ fractionation factors are calculated for a selection of minerals and molecules, using first-principles density functional theory models to estimate vibrational frequencies, with a particular focus on investigating the potential for detectable signatures of high-temperature equilibrium processes. Reduced partition function ratios as well as mass-fractionation exponents are tabulated versus temperature. The results are compared with previous theoretical studies, laboratory experiments, and field-based calibrations. Effects of nuclear field shift isotope fractionation and double-well potential anharmonicity on the relationship between $^{18}O/^{16}O$ and $^{17}O/^{16}O$ are also investigated. The estimated field shift effect is much smaller than mass-dependent fractionation, yielding no more than 1 per meg in measured $\Delta'^{17}O$ at 25°C, and correspondingly less at higher temperatures. Anharmonic vibration in a double-well potential, such as might be found in a Si–O–Si linkage in polymerized silicates, also does not seem to generate dramatic $\Delta'^{17}O$ signatures for plausible potential shapes, and non-Born–Oppenheimer effects on $\Delta'^{17}O$ signatures also appear to be limited. None of the studied effects appear likely to generate the negative $\Delta'^{17}O$ anomalies observed in polymerized silicate mineral samples from high-temperature rocks on the Earth & Moon.

$\Delta^{17}O$ signatures of equilibrium processes

Large mass-independent fractionation signatures in oxygen, sulfur, and mercury isotopes in natural samples are well known, and are generally thought to result from a restricted set of disequilibrium reaction processes including photochemistry and molecular recombination (e.g. Heidenreich and Thiemens 1986; Mauersberger 1987 for ozone; Clayton et al. 1973; Mc Keegan et al. 2011 for early solar system materials; Farquhar et al. 2000, for the Archean sulfur cycle; Bergquist and Blum 2007, for mercury). Over the last two decades, possible uses of subtle variability in the mass-dependence of isotope fractionation caused by more mundane processes have become a topic of broad interest in geochemistry (e.g., Young et al. 2002; Deines 2003; Farquhar et al. 2003; Barkan and Luz 2005; Rumble et al. 2007; Luz and Barkhan 2010; Cao and Liu 2011 ; Levin et al. 2014; Pack and Herwartz 2014; Passey et al. 2014; Bao et al. 2015; Dauphas and Schauble 2016). Variation in the mass dependence of equilibrium stable isotope fractionation has long been predicted (e.g., Grilly 1951; Hulston and Thode 1965; Matsuhisa et al. 1978), but this phenomenon has not been widely exploited in geochemical studies until recently.

It is now recognized that measurements of variations in the mass dependence of equilibrium oxygen isotope fractionation may help in geochemical determinations of the formation temperatures of mineral precipitates as well as characterization of parent solutions (Cao and Liu 2011 ; Levin et al. 2014; Pack and Herwartz 2014; Passey et al. 2014; Sharp et al. 2016).

So far, most work on the mass dependence of equilibrium oxygen isotope fractionation has focused on the hydrological cycle, and the precipitation of carbonates and silica from aqueous solution. Cao and Liu (2011) made the first detailed theoretical study, using molecules and molecular analogues of carbonate and silicate structures in crystals and solution. This work focused on estimating the scaling relationships between $^{18}O/^{16}O$ and $^{17}O/^{16}O$ fractionations for different species depending on temperature, i.e.,

$$\theta_{a-b}(T) = \ln^{17/16}\alpha_{a-b}/\ln^{18/16}\alpha_{a-b} \qquad (1)$$

$$\Delta'^{17}O_{a-b}\ (\text{‰}) = 10^3\ (\ln^{17/16}\alpha_{a-b} - \theta_{ref}\ \ln^{18/16}\alpha_{a-b}) \qquad (2)$$

where θ_{a-b} is the mass-fractionation exponent for substance "a" relative to substance "b", $^{17/16}\alpha_{a-b}$ is the equilibrium $^{17}O/^{16}O$ fractionation factor, $^{18/16}\alpha_{a-b}$ is the equilibrium $^{18}O/^{16}O$ fractionation factor, and θ_{ref} is a reference exponent (typically but not always chosen to be 0.528). $\Delta'^{17}O_{a-b}\ (\text{‰})$ is used here to mean a differential measure of the $^{17}O/^{16}O$ ratios in the two substances, relative to what would be predicted by the reference exponent—equivalent to what is sometimes called $\Delta\Delta'^{17}O_{a-b}$—and it is not referred to a particular isotope standard material. Bao et al. (2015) made a generalized statistical study of mass dependence in hypothetical systems for both equilibrium and kinetic processes, showing the expected limits of mass-dependence for chemically plausible materials. Most recently, Hayles et al. (2018) modeled $^{18}O/^{16}O$ and θ_{a-b} for quartz, carbonates, apatite, magnetite, and water using molecular-cluster methods, and Liu et al. (2019) modeled $^{18}O/^{16}O$ and θ_{a-b} in the sulfate minerals gypsum and basanite. Guo and Zhou (2019) and Hill et al. (2020) calculated $^{18}O/^{16}O$ and θ_{a-b} for water, CO_2, Dissolved Inorganic Carbon (DIC), and carbonate minerals. Guo (2020) also examined potential signatures of kinetic processes on $\Delta'^{17}O_{CaCO_3-H_2O_{(l)}}$.

There is tantalizing evidence of seemingly unexplained $\Delta'^{17}O$ values for some high-temperature minerals on the Moon and on Earth (Fig. 1) at the ~10 to 20 per meg level. In particular, some tectosilicates exhibit lower $\Delta'^{17}O$ values than their more mafic counterparts. A striking example is the low $\Delta'^{17}O$ values for both terrestrial and lunar anorthosites (Fig. 1). The low $\Delta'^{17}O$ values for lunar anorthosites, ferroan anorthosites, and troctolites is a robust measurement made by numerous workers spanning two decades (e.g, Wiechert et al. 2001; Young et al. 2016, Cano et al. 2020). Relationships like those in Figure 1 are seen in other terrestrial data (e.g., Pack and Herwartz 2014). The correlation hints at a crystal chemical control on $\Delta'^{17}O$, with tectosilicates generally exhibiting lower $\Delta'^{17}O$ values than less polymerized silicate minerals. For example, a rough correlation between $\Delta'^{17}O$ and bulk modulus is suggested; tectosilicates have both low $\Delta'^{17}O$ and lower bulk moduli than orthosilicates, and the analyses summarized in Figure 1 suggest that quartz may have lower $\Delta'^{17}O$ values than less compressible plagioclase feldspars. Similar trends are obtained using thermal expansivity, and the distinctive effect for tectosilicates could be related to the nature of the 3-D framework of corner-sharing SiO_4 tetrahedra.

Analyses of this type at sufficient analytical precision are not yet plentiful enough to ascertain their veracity by interlaboratory comparisons. As an example of potential analytical pitfalls, Pack et al. (2016) found a non-linearity in $\Delta'^{17}O$ vs. $\delta'^{18}O$ of ~ 1 per meg/per mil specific to their mass spectrometer. However, correcting for this effect is not sufficient to remove the correlation between $\Delta'^{17}O$ and crystal chemistry. As new technologies become available (larger gas-source mass spectrometers, better collection systems), this trend will be scrutinized. In the meantime, we consider it prudent to investigate possible explanations for what would seem to be unexpected disparities in $\Delta'^{17}O$ values among high temperature minerals.
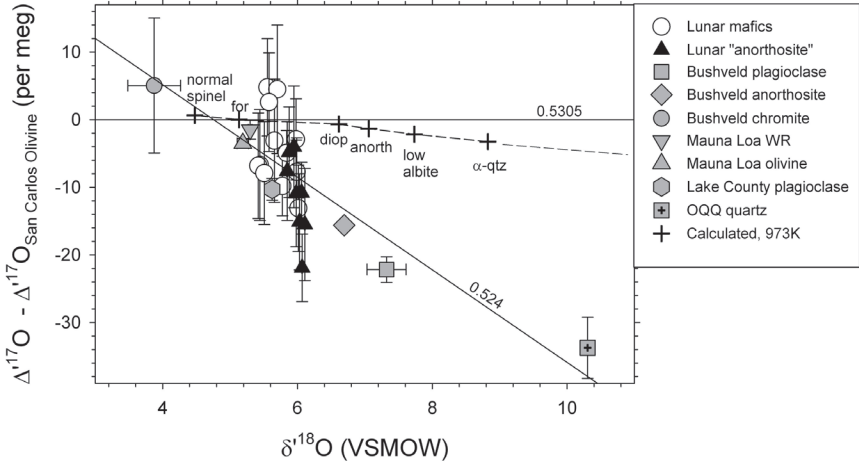
Figure 1. Triple oxygen isotope ratio analyses of lunar and terrestrial samples compared with the estimates obtained in this study. Each datum is expressed as $\Delta'^{17}O$ relative to San Carlos olivine vs. $\delta'^{18}O$ relative to VSMOW. For comparison, the calculations for α-quartz, low albite, anorthite, diopside and normal spinel from this study are normalized to the $\Delta'^{17}O$ coexisting forsterite and the $\delta'^{18}O$ of San Carlos olivine. Lunar and terrestrial anorthosites have low $\Delta'^{17}O$ values compared with basalts and other mafic lunar and terrestrial mineral separates. Terrestrial samples include feldspar and spinel separated from a diabase from the Bushveld complex, anorthosite from the Bushveld, Lake County plagioclase, a commonly used plagioclase standard material, and a whole-rock and olivine sample from a Mauna Loa basalt. Also shown is an analysis of the Oliver Quarry Quartz (OQQ), a quartz oxygen isotope standard, with a similar precision showing that it too has low $\Delta'^{17}O$ values relative to terrestrial mantle and to lunar and terrestrial basalt. Two mass fractionation lines defined by the exponent for triple oxygen isotope fractionation are shown for reference. One is for the theoretical high-temperature maximum exponent of 0.5305 and the other is for a value of 0.524. All analyses performed at the laboratory at UCLA using CO_2 laser heating assisted fluorination (e.g., Young et al. 2016).

One possibility, explored here, is that there are anomalous and significant mass-dependent effects based on crystal chemistry, and anharmonicity in particular, even in systems equilibrated at igneous or high-grade metamorphic temperatures. However, other explanations have been put forward. Cano et al. (2020) suggested that variable $\Delta'^{17}O$ values for lunar samples are the result of a mass-independent effect carried by vapor early in the Moon's history, followed by exchange of this vapor reservoir with the precursors to the lunar crust, including the anorthosites and troctolites. The suggestion is that identical $\Delta'^{17}O$ values for lunar and terrestrial basalts is serendipitous. Additional possibilities include pervasive, incipient alteration of feldspars in the terrestrial environment and analytical artifacts related to fluorination. The latter would be consistent with an historical difficulty in analyzing alkali feldspars by laser-assisted fluorination methods.

Motivated by these observations and their potential importance, this chapter aims to assemble a broad survey of equilibrium isotope fractionation factors and mass fractionation exponents for geochemically significant minerals using a consistent computational method. We attempt to estimate both $^{18}O/^{16}O$ fractionations and θ exponents with reasonable accuracy. In order to avoid extraneous terminology, we generally adopt the notation scheme of Cao and Liu (2011) with one minor simplification. We describe the mass fractionation exponent between a substance a and an ideal gas of O-atoms as $\theta_{a-atoms}$, analogous to θ_{a-b}, rather than using the Greek letter κ. We have also chosen to place some additional emphasis on the estimation of changes in $\Delta'^{17}O$ resulting from equilibrium fractionation. The relationship defined by Cao and Liu (2011) between $\theta_{a-atoms}$, $\theta_{b-atoms}$, and θ_{a-b} is then written:

$$\theta_{a-b} = \theta_{a-atoms} + (\theta_{a-atoms} - \theta_{b-atoms})\ln{}^{18/16}\beta_b/\ln{}^{18/16}\alpha_{a-b} \tag{3}$$

here β_b is the reduced partition function ratio for β and their relationship with $\Delta'^{17}O_{a-b}$ (‰) becomes (Dauphas and Schauble 2016):

$$\Delta'^{17}O_{a-b}\ (‰) = 10^3\ (\theta_{a-atoms}\ \ln^{18/16}\beta_a - \theta_{b-atoms}\ \ln^{18/16}\beta_b - \theta_{ref}\ \ln^{18/16}\alpha_{a-b}) \tag{4}$$

$\Delta'^{17}O$ has the advantage that it remains bounded (and small) near crossovers; i.e., where $\ln^{18/16}\alpha_{a-b}$ approaches zero, and is more intuitively relatable to measurable deviations in mass dependence where $^{18/16}\alpha_{a-b}$ is close to unity. Unless otherwise specified, we assume $\theta_{ref} = 0.528$, in keeping with most prior studies. Because of the overlap with Hayles et al. (2018) in materials studied, we will make a particular effort to compare their results with the present models.

Most theoretical studies of equilibrium stable isotope fractionation are based on the assumption that molecular and crystalline vibrational frequencies may be treated harmonically; though some recent studies have investigated anharmonic effects (Liu et al. 2010; Webb and Miller 2014; Pinella et al. 2015; Dupuis et al. 2017). Cao and Liu (2011) concluded that anharmonicity was not likely to have a major effect on the mass dependence of equilibrium fractionation in typical molecules.

However, not all potentially relevant types of anharmonic potential have been examined. A secondary goal of the present study is to examine the effects of anharmonicity involving double-well potentials on the mass dependence of fractionation. This type of potential was not specifically tested in the studies cited above, but double-well potentials may be relevant to understanding systems with hydrogen bonding (such as in liquid water; e.g., Tachikawa and Shiga 2005) as well as oscillations involving Si–O–Si and Si–O–Al angles in polymerized silicate structures (e.g., Dove et al. 1995). These examples share the common property that there are two "stable" asymmetric configurations with associated potential minima that are separated by a potential barrier. For Si–O–Si the asymmetry, at its simplest, is caused by the greater stability of a crooked bond angle relative to a linear configuration with a 180º Si–O–Si bond angle. For hydrogen bonding, asymmetry comes from the preference for hydrogen to be nearer to one oxygen than to the other. Double-well potentials have distinct quantum-mechanical properties, including splitting of energies and delocalization. Whether these might influence the mass dependence of fractionation is an interesting question.

Other equilibrium phenomena that may influence observed signatures are also discussed, including nuclear field shifts and non-Born–Oppenheimer effects. These effects are discussed in more detail in the following section.

PREDICTING $^{17}O/^{16}O$ SIGNATURES

Estimating mass-dependent fractionations in the harmonic approximation

In this chapter, mass fractionation laws for crystals and molecules are calculated theoretically using vibrational (phonon) spectra modeled with density functional theory. The harmonic oscillator approximation of the vibrational contribution to the Helmholtz free energy (i.e., Bigeleisen and Mayer 1947) is assumed, unless otherwise noted. Isotopic effects on the free energy are determined by comparing a series of models with isotopic substitution of ^{16}O, ^{17}O, and ^{18}O on each crystallographically distinct oxygen site. Each heavy-isotope substituted model in the series contains an ^{17}O or ^{18}O substitution on a single atom per unit cell. In some cases, the perturbation associated with a phonon wave vector leads to the loss of symmetry. In these cases, single atom isotope substitutions are performed on multiple positions corresponding to the same crystallographic site in order to obtain a complete sample over the unit cell. The total fractionation factor for each isotope in the crystal is then determined by the weighted arithmetic average of the single-atom substitutions involving that isotope. We report the result as a fractionation factor relative to an ideal gas of oxygen atoms, analogous to the reduced partition function ratio.

Note, however, that this definition of β is slightly different than is commonly found in older literature, where β is determined from the vibrational frequencies of a substance with complete substitution of ^{18}O or ^{17}O for ^{16}O, rather than as the weighted average of many independent single-atom substitutions. Cao and Liu (2011) have shown that mass law estimations are inaccurate when the rule of the mean is applied to β determined in completely substituted isotopologues.

Here we focus on models with periodic boundary conditions, for crystalline mineral phases, constructed using density functional theory. Molecular and cluster-based models have also been used to assess mass dependence in crystalline phases (e.g., Cao and Liu 2011; Hayles et al. 2018). An important advantage of molecular and cluster-based methods is that highly accurate electronic structure methods are more easily applied. However, an important disadvantage is the need to truncate such models at some finite number of atoms, introducing edge effects and complicating comparisons with relevant experimental data such as Raman spectra. Comparing results from both model types against each other is one way to test their relative merits. Ultimately it appears that both approaches yield similar results for most phases. The new model results reported here are based on the Perdew et al. (1996) gradient corrected density functional, abbreviated PBE. PBE is a widely used functional, including for previous studies of equilibrium isotope fractionation and related effects (e.g., Schauble et al. 2006; Meheut et al. 2007).

Pseudopotentials and Projector Augmented Wave (PAW) datasets are used in this study, greatly reducing the computational complexity of periodic boundary condition models by simplifying the treatment of both inner-shell and valence electrons; in recent years several public repositories of well-designed pseudopotentials and PAW datasets have become available, covering most elements in the periodic table. However, the application of these repositories to isotope fractionation calculations is still in need of testing. Here, anhydrous, carbon-free crystals are modeled primarily using ultrasoft pseudopotentials from the GBRV library (Garrity et al. 2014; including updates through version 1.5). An important parameter in pseudopotential-based calculations is the cutoff energy of the plane-wave basis set—in general a higher cutoff energy allows for more accurate representation of chemical bonds, while also increasing the computation time, and a range of cutoff energies should be tested to achieve a balance between convergence and efficiency in the system of interest. As a general matter, the choice of cutoff will be dependent on the pseudopotential, the electronic structure of the material, and the desired accuracy. The GBRV pseudopotential family is notable for tolerating relatively low cutoff energies across a broad range of elements (Garrity et al. 2014). Our testing with GBRV pseudopotentials indicated that an energy cutoff of 40 Rydberg (544 eV) was sufficient for the crystals studied here (Table 1). Models of $LaPO_4$ in the monazite structure and $LuPO_4$ in the xenotime structure used rare-earth element PAW data sets developed by Topsakal and Wentzcovitch (2014); these models had somewhat higher energy cutoffs of 55 Rydberg and 45 Rydberg, respectively, as recommended in testing done by the Standard Solid State Pseudopotential project (http://materialscloud.org/sssp). Hydrous and carbon-bearing crystals and molecules are modeled using a mixture of pseudopotentials drawn mainly from the GBRV and PSLibrary pseudopotential libraries, crudely following the recommendations of the Standard Solid State Pseudopotentials project (Dal Corso 2014; Lejaeghere et al. 2016; Prandini et al. 2018, with a higher energy cutoff of 80 Rydberg (1088 eV). All DFT calculations were made using version 5.4 of the Quantum Espresso software package (Giannozzi et al. 2009; http://www.quantum-espresso.org).

Having chosen a functional, pseudopotential, and energy cutoff, the next important parameter is the grid over which electronic wave vectors are sampled. A finer grid will give a more accurate depiction of the actual electronic structure, but also slow calculations down and limit the complexity of crystals that can be modeled. Test calculations indicate that a range of one to 20 discrete electronic wave vectors can make a sufficiently accurate grid,

Table 1. Pseudopotentials used in the present study.

Element	GBRV-based models	Ref.	PSLibrary/SSSP-based models	Ref.
H	h_pbe_v1.4.uspp.F.UPF	1	H.pbe-rrkjus_psl.0.1.UPF	3
C	c_pbe_v1.2.uspp.F.UPF	1	C.pbe-n-kjpaw_psl.1.0.0.UPF	3
N	n_pbe_v1.2.uspp.F.UPF	1	N.pbe.theos.UPF	4
O	o_pbe_v1.2.uspp.F.UPF	1	O.pbe-n-kjpaw_psl.0.1.UPF	3
F	f_pbe_v1.4.uspp.F.UPF	1		
Na	na_pbe_v1.5.uspp.F.UPF	1	unchanged	1
Mg	mg_pbe_v1.4.uspp.F.UPF	1	unchanged	1
Al	al_pbe_v1.uspp.F.UPF	1	Al.pbe-n-kjpaw_psl.1.0.0.UPF	3
Si	si_pbe_v1.uspp.F.UPF	1	Si.pbe-n-rrkjus_psl.1.0.0.UPF	3
P	p_pbe_v1.5.uspp.F.UPF	1	P.pbe-n-rrkjus_psl.1.0.0.UPF	3
S	s_pbe_v1.4.uspp.F.UPF	1	unchanged	1
Cl	cl_pbe_v1.4.uspp.F.UPF	1	Cl.pbe-n-rrkjus_psl.1.0.0.UPF	3
K	k_pbe_v1.4.uspp.F.UPF	1	K.pbe-spn-rrkjus_psl.1.0.0.UPF	3
Ca	ca_pbe_v1.uspp.F.UPF	1	unchanged	1
Y	y_pbe_v1.4.uspp.F.UPF	1	unchanged	1
Zr	zr_pbe_v1.uspp.F.UPF	1	Zr.pbe-spn-kjpaw_psl.1.0.0.UPF	3
Ba	ba_pbe_v1.uspp.F.UPF	1		
La	La.GGA-PBE-paw-v1.0.UPF	2		
Lu	Lu.GGA-PBE-paw-v1.0.UPF	2		

Pseudopotential References:
1. GBRV: Garrity et al. (2014); https://www.physics.rutgers.edu/gbrv/
2. Wentzcovitch et al. (2014); http://www.vlab.msi.umn.edu/resources/repaw/index.shtml
3. PSLibrary: Dal Corso et al. (2014); http://people.sissa.it/~dalcorso/pslibrary/index.html.
4. THEOS: http://materialscloud.org/sssp

depending on the size and symmetry of a particular crystal's unit cell. A detailed discussion of the choice and testing of wave-vector grids is beyond the scope of this review, and different researchers commonly make different choices for the same crystal structure. In principle, any sufficiently dense grid should yield a similar result. Because of the large range of materials studied here, it was decided to adopt a standard procedure for choosing grids: they are chosen so that the shortest real-space vector that belongs to the reciprocal of the wave-vector lattice formed by each grid is approximately 35 Bohr radii (~19 Å) or longer. The idea of a vector-length metric for evaluating grid accuracy was proposed by the developers of the ABINIT DFT software package (www.abinit.org), though they do not specify the 35 Bohr threshold—this choice would indeed not be appropriate other types of materials: electronically conductive metals require finer grids, for instance. Our own parameter testing suggests that the 35 Bohr criterion is adequate to ensure convergence of unit-cell lengths at the ~0.1% level for the materials studied here, with reasonable consistency in calculated phonon frequencies. For each crystal, a thermodynamically representative sample of phonon frequencies is calculated using a somewhat coarser grid of phonon wave vectors, typically with a vector-length metric of approximately 19 Bohr radii (~10 Å). Both phonon and electronic wave vector grids are chosen to give good convergence in calculated isotopic fractionation and crystal structures at relevant temperatures. Similar tests have been described in previous studies (e.g., Elcombe and Hulston 1975; Schauble et al. 2006; Meheut et al. 2007, and others).

Phonon frequencies—the crystal analogue of molecular vibrational frequencies—are typically underestimated by several percent by the Perdew et al. (1996) functional. This is important because the calculation of equilibrium stable isotope fractionation depends on the differences in frequencies between isotopically substituted materials (Biegeleisen and Mayer 1947). In order to partially correct for this systematic error, a frequency scale factor of 1.043 has been applied in all fractionation calculations; the scale factor is determined by a proportional regression of calculated phonon frequencies correlated with frequencies measured with Raman, infrared, and neutron spectroscopy (Fig. 2). This scale factor is similar to previous determinations for PBE-based models of periodic models of silicates, oxides and carbonates (e.g., Schauble et al. 2006, 2011; Meheut and Schauble 2014; Widanagamage et al. 2014). It should be noted that scale factors determined by general-purpose benchmark studies of the vibrational frequencies of small molecules (e.g., Merrick et al. 2007 and references therein) are typically closer to unity. However, in these studies larger scale factors (similar to ours) are found for low-frequency vibrational modes ($< \sim 1000 \text{cm}^{-1}$, depending on the study). This lower frequency range is much more common in the crystals studied here than in molecular data sets, and frequencies less than 1200 cm^{-1} dominate our overall fit. Larger low-frequency scale factors appear to be typical for gradient-corrected functionals (such as PBE) as well as for hybrid methods that include a gradient-corrected functional component (such as B3LYP; Becke 1993); e.g., Merrick et al. (2007). Further details of the scale factor determination are presented in the following section.
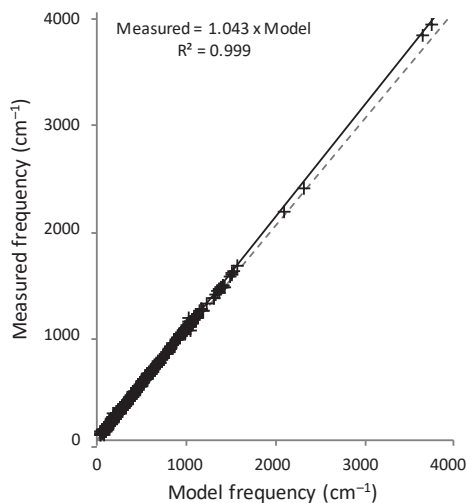

Figure 2. Vibrational frequency correlations with Raman, infrared, and inelastic neutron scattering measurements for estimating the frequency scale factor. In general, OH stretching and bending frequencies are not included in the correlation because of the larger anharmonic effects expected for these modes. Frequencies in H_2O, CO_2, and CO vapor are compared with empirically estimated harmonic frequencies, all other correlations are with measured fundamental frequencies. References for measured frequencies: α-quartz – Castex and Maddon (1995); albite – Aliatis et al.(2015); microcline – Zhang et al. (1996); diopside – Prencipe et al. (2012); jadeite – Prencipe et al. (2014); forsterite – Kolesov and Geiger (2004); zircon – Chaplot et al. (2006); grossular – Maschio et al. (2014); spinel – Chopelas and Hofmeister (1991); lizardite – Hofmeister and Bowey (2006); xenotime-Y – Giarola et al. (2011); xenotime-Lu – Mittal et al. (2007); monazite-La – Begun et al. (1981) and Geisler et al. (2016); fluorapatite – Leroy et al. (2000); anhydrite – Berenblut et al. (1973) and Iishi (1979); barite – Dawson et al. (1977) and Jayasooriya et al. (1996); gypsum – Iishi (1979); $NaClO_4$ – Lutz et al. (1979) and Toupry-Krauzman et al. (1978); calcite – Pavese et al. (1992); aragonite – Carteret et al. (2013); dolomite – Pilati et al. (1998) and Gillet et al. (1993); magnesite – Rutt and Nicola (1974) and Hellwege et al. (1970); nahcolite – Bertoluzza et al. (1981); nitratine – Yamamoto et al. (1976), Brehat and Wyncke (1985), Eckhardt et al. (1970), and Lefebvre et al. (1980); H_2O vapor – Benedict et al. (1956); CO_2 – Zuñiga et al. (2001); CO – Mantz and Maillard (1975).

During model testing, it became clear that pseudopotentials from the GBRV library are reliable, fast, and accurate for calculations on anhydrous, carbon-free crystals. However, hydrous materials and molecules with short, covalent bonds are more problematic—this group includes water vapor, carbon monoxide, and carbon dioxide. GBRV models overestimate O–H stretching frequencies in water vapor, the water vapor dimer $(H_2O)_2$, silicic acid vapor (H_4SiO_4) and disilicic acid vapor $(H_6Si_2O_7)$ by ~90–100 cm^{-1}, and the asymmetric C–O stretching frequencies in carbon dioxide and carbon monoxide by ~40–50 cm^{-1}, relative to benchmark calculations with the PBE functional and large atom-centered Gaussian basis sets (e.g, aug-cc-pVTZ). Large Gaussian basis sets such as these should approach the greatest possible accuracy achievable with the PBE functional, when applied to molecules. When tested in periodic boundary condition calculations of hydroxyl-bearing and hydrate minerals, we find that PBE-GBRV models show offsets of 10's of cm^{-1} relative to the alternative pseudopotentials, suggesting that the artifacts are not limited to molecules modeled *in vacuo*. In contrast, other pseudopotential libraries show much closer matches to the Gaussian basis set results, suggesting that this is a problem isolated to the O- and H- (and to some extent C-) pseudopotentials in the GBRV library, which were designed to optimize computational speed as well as accuracy. We have generated alternative models using a mixture of pseudopotentials drawn mainly from the GBRV and PSLibrary pseudopotential libraries, because they match benchmark calculations for molecules more closely (rms errors of < 10 cm^{-1} for CO, CO_2, H_2O and the H_2O dimer, and ~13 cm^{-1} for silicic and disilicic acid vapor). Both GBRV and alternative pseudopotentials yield very similar phonon frequencies in anhydrous, carbon-free crystalline phases, with indistinguishable scale factors and residual root-mean-square (rms) errors after scaling. Models using the alternative pseudopotential set are considerably more computationally demanding than GBRV-based models, mainly because they require a higher energy cutoff. This limits their practical application to phases with relatively simple and compact unit cells. In general, we observe that the choice of GBRV vs. alternative pseudopotentials has a negligible effect on both fractionation factors and mass law exponents for anhydrous crystals. For hydrous species and molecules, the choice of pseudopotentials has only a modest effect on the mass fractionation exponent $\theta_{a-atoms}$, but often substantial effects on estimated $^{18}O/^{16}O$ fractionation factors—up to several per mil at room temperature. We therefore report results using the alternative pseudopotentials for molecules, carbonates, and hydrous crystals, but GBRV results for anhydrous, carbon-free phases, even though we originally intended to focus on GBRV results for all materials studied.

Molecules are treated in much the same way as crystals, with the exception of H_2O, CO_2, and CO vapor. Harmonic frequencies and anharmonicity parameters have been determined for each of these molecules on the basis of detailed spectroscopic measurements, making more sophisticated (and presumably more accurate) fractionation factor estimates possible (e.g., Urey 1947; Richet et al. 1977; Rosenbaum 1997). Although there is disagreement about the best compromise between practicality and accuracy in incorporating anharmonic effects into isotope fractionation factor calculations, Urey (1947), Richet et al. (1977), Liu et al. (2010), and others have confirmed that the anharmonic effect on vibrational zero-point energy is typically the most significant correction. Therefore, we determined molecule-specific scale factors for each of these molecules by fitting model frequencies to previously determined harmonic frequencies for the dominant isotopologue, and applied a correction for anharmonicity in the calculation of $\ln^{18/16}\beta$ by adjusting the zero-point energy term in the equation for the reduced partition function ratio (Urey 1947; Rosenbaum 1997). Anharmonic zero-point energies are estimated with the perturbational VPT2 method (Barone 2005) using the PBE functional and aug-cc-pVQZ basis sets (Kendall et al. 1992), as implemented in the Gaussian 09 software package (Frisch et al. 2013). An alternative anharmonic method, CC-VSCF in the quartic force field approximation (Yagi et al. 2004) was also tested. Both methods give similar results for CO and CO_2, but CC-VSCF appears to somewhat underestimate the anharmonicity of

H_2O vibrations, leading to $\sim 0.7\%o$ higher estimated $\ln^{18/16}\beta$ at 298 K. VPT2 anharmonicity parameters for H_2O, in contrast, come close to spectroscopic determinations (Benedict et al. 1956, and subsequent studies). We find substantially improved agreement with previous estimates of $^{18}O/^{16}O$ fractionation factors and $\ln^{18/16}\beta$ using this correction method.

In all cases, $\theta_{a-atoms}$ is calculated using the harmonic oscillator assumption (Cao and Liu 2011). In agreement with the earlier study, we find limited effects of anharmonicity on the mass dependence exponent of fractionation. Compared to the anharmonicity-corrected zero-point energy method described above, a purely harmonic determination of $\theta_{CO_2-atoms}$ is within $\sim 2 \times 10^{-5}$ from 273–1573 K; for $H_2O(v)$ the difference is less than 1×10^{-5} below 1273 K. The simplified anharmonic correction procedure is not thermodynamically self-consistent because rotational and excited vibrational state energies do not arise from the same potential as the ground state (zero point) energy, and this introduces a (likely very small) artifact in θ that we prefer to avoid. For the sake of consistency, a harmonic $H_2O(v)$ model using the crystal frequency scale factor is used for estimating fractionations relative to ice and the hydration water of gypsum. The harmonic model predicts 2–3‰ higher $^{18}O/^{16}O$ than the anharmonicity-corrected model over the temperature range 273–373 K (0–100 °C).

Our model for liquid and supercritical water is based on the model for water vapor, modified by adding $10^3 \ln^{18/16}\alpha_{liquid-vapor}$ from Rosenbaum (1997) to $10^3 \ln^{18/16}\beta_{water\,vapor}$. $\theta_{liquid\,water-atoms}$ is estimated three different ways:

1. by applying $\theta_{liquid\,water-water\,vapor} = 0.529$, as measured by Barkan and Luz (2005);

2. by taking the lower of $\theta_{liquid\,water-atoms}$ as calculated by (1) and $\theta_{water\,vapor-atoms}$, in the expectation that condensed water will never have θ below the vapor, and

3. by taking a simple average of $\theta_{water\,vapor-atoms}$ and $\theta_{ice\,Ih-atoms}$, based on the observation that predicted ice–vapor $^{18}O/^{16}O$ fractionation at 273 K is roughly twice as large as the observed liquid–vapor fractionation, and fractionations for both phases relative to water vapor are driven by similar H-bonding interactions.

Methods (1) and (3) are crudely analogous to the "semi-empirical" and "ab initio" approaches taken by Hayles et al. (2018) in that they incorporate empirical $\theta_{liquid\,water-water\,vapor}$ estimates in the first case, and *ab initio* model results for clusters of water molecules in the second case. In practice, the choice of estimation method does not matter very much at low to moderate temperature—the various phases of H_2O stay close to the limiting harmonic value of $\theta_{water-atoms} \approx 0.530$ regardless of the details of the theoretical treatment, and the three methods outlined above agree to within 1×10^{-4} from 263–673 K (–10 °C to 400 °C). Above 400 °C, a naïve application of method (1) (i.e., assuming a supercritical fluid–vapor exponent of 0.529 even though the temperatures are far above those studied by Barkan and Luz) yields rapidly increasing $\theta_{liquid\,water-atoms}$, eventually reaching unrealistically high values. For this reason, results from methods (2) or (3) are probably more reliable for higher temperatures; (2) and (3) are also in good agreement with each other in this temperature range. Note that an alternative parameterization of the liquid–vapor fractionation parameterization has been proposed by Horita and Wesolowski (1994). Their fitted fractionation curve is generally quite close to that of Rosenbaum (1997) up to the critical temperature of water, and the choice of one model over the other has little effect on our results at most temperatures.

At this time, it is simply not possible to routinely determine anharmonic parameters for crystals with significant structural complexity. However, the practical impact of this restriction may be limited because the vibrational thermodynamics of H_2O are more strongly affected by anharmonicity than typical materials, and because the general scale factor determination for crystals is fitted to fundamental frequencies. Fundamental frequencies will typically deviate from harmonic frequencies in the same direction as the anharmonic zero-point energy

correction, albeit by a slightly larger magnitude, and so the crystal models will already tend to overestimate this component of the anharmonic effect.

Crystal structures calculated with the PBE functional and pseudopotentials are compared with structures measured by X-ray and neutron-diffraction in Table S1 in the Supplemental Information. In general, unit cell volumes are overestimated by approximately 3%, as is typical for the PBE functional. Calculated phonon frequencies are compared with Raman, infrared, and inelastic neutron-scattering measurements in Table S2 and Figure 2. In general, model and measured frequencies are in excellent agreement after applying the fitted scale factor, with a root-mean-square misfit of 13 cm^{-1}, compared to a root-mean-square frequency of about 689 cm^{-1}, indicating an average scatter of roughly 2%. We have included the molecules H_2O, CO_2 and CO in this scale factor fit, so as to sample as wide a range of bond environments as possible, but have correlated harmonic frequencies rather than fundamentals for these molecules. In practice, these three molecules represent relatively few modes, so their impact on the calculated scale factor is modest (1.043 with molecules, vs. 1.045 without). It should be noted that almost all correlated phonons correspond to a near-zero wave vector, and that other parts of the Brilluoin Zone might conceivably show larger misfits or different scaling. However, there are relatively few studies that probe non-zero wave vectors, particularly in the higher-frequency range that mainly controls O-isotope fractionation (Kieffer 1982). Overall, vibrational frequency correlations suggest that the models will be able to make useful estimates of mass-dependent equilibrium isotope fractionations and mass dependence exponents. Likely uncertainties in these estimates arising will be discussed in more detail below.

Effects beyond the harmonic approximation

Anharmonicity in a double-well potential. To extend earlier work on the effects of anharmonicity on the mass dependence of fractionation (e.g., Cao and Liu 2011), a highly simplified model system consisting of a one-dimensional quantum oscillator in a double-well potential is investigated. The potential is assumed to take the form of a harmonic potential that is perturbed by a central Gaussian peak ($V = V_0 + k_{fc}x^2/2 + b\,e^{-cx^2}$) where k_{fc} is the harmonic spring constant, b determines the height of the Gaussian perturbation, and c controls the width of the Gaussian perturbation (c here should not be confused with the speed of light). This is only one of many possible types of double-well potentials, but it has two important advantages for the present purpose:

1. the ground state and many low-lying excited state energies can be calculated quickly with high precision, and

2. the potential and its solutions converge to the well-understood harmonic oscillator in both the limit of small perturbations ($b/k_{fc} \to 0$, and/or $c \to \infty$) and in the limit of high energy: $E_n \to h\nu_{harmonic}\,(n + 1/2)$ as $n \to \infty$, where $\nu_{harmonic} = (k_{fc}/m)^{1/2}/(2\pi)$ is the characteristic vibrational frequency of the harmonic part of the potential.

Solution of the Schrödinger equation for this potential is simplified by substituting parameters scaled to the characteristic frequency $\nu_{harmonic}$, i.e. $B = b/(h n_{harmonic})$ for the height of the Gaussian above the minimum of the harmonic potential, $\gamma = ch/(m\nu_{harmonic})$ for the sharpness of the Gaussian, and $y = x(mn\nu_{harmonic}/h)^{1/2}$ for the positional coordinate. In the present work, the Schrödinger equation for this potential is solved via the matrix method of Earl (2008), using Scilab (v. 6.0.0). Accurate eigenvalues corresponding to energy states up to $n = 73$ are obtained in roughly one CPU-minute per potential on a laptop computer by solving separate 49×49 matrices for even and odd quantum numbers. Such matrices actually yield estimates of energies for states up to $n = 97$, but the highest energy states are poorly converged because of the truncation of higher-order terms that would require larger matrices (i.e., the energies typically varied by ~10^{-5} $h\nu_{harmonic}$ or more in test calculations with $B = 1$–5 between 49×49, 48×48, and 47×47 matrix solutions). Representative examples of

a.

$\gamma = 1$

—	B = 10
—	B = 5
—	B = 2
—	B = 1
—	B = 0.5
—	B = 0

Potential Energy

Distance

b.

B = 5

—	$\gamma = 5$
—	$\gamma = 2$
—	$\gamma = 1$
—	$\gamma = 0.5$
—	$\gamma = 0.2$
—	$\gamma = 0.1$

Potential Energy

Distance

c.

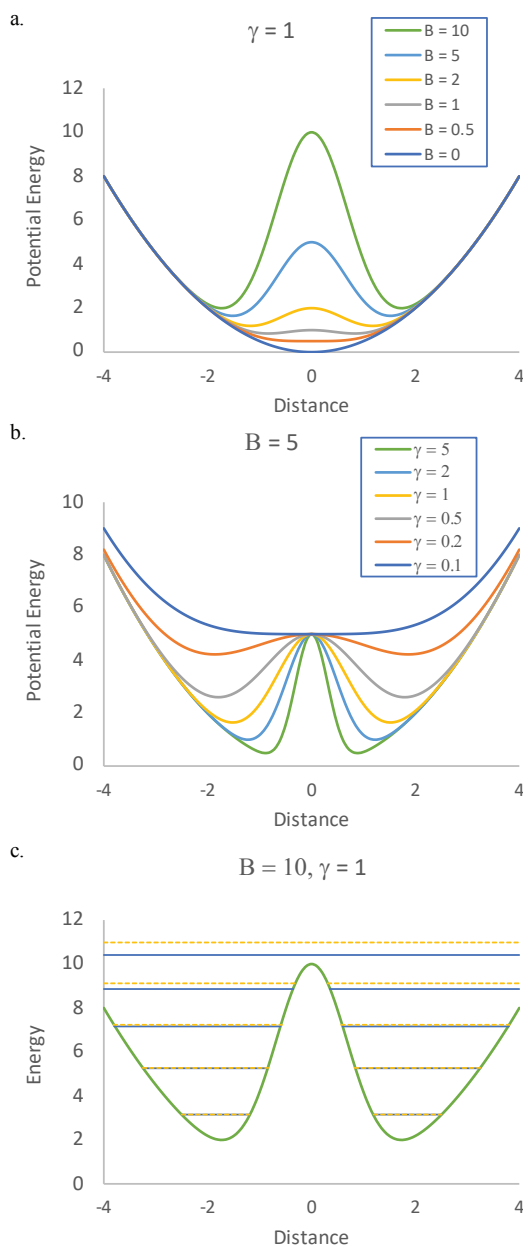$B = 10, \gamma = 1$

Energy

Distance

Figure 3. Examples of double-well potentials consisting of a central Gaussian peak within a harmonic potential. The potential and distance units are scaled with respect to the quanta of the harmonic component of the potential, as described in Earl (2008). **a)** Variation in peak height (*B*). **b)** Variation in the sharpness of the central Gaussian (γ). **c)** Quantum energy levels in an example potential. **Solid horizontal lines** represent the lowest even quantum numbers *n* = 0, 2, 4, 6, and 8; **dashed horizontal lines** represent odd quantum numbers *n* = 1, 3, 5, 7, and 9.

potentials and calculated vibrational energies corresponding to different values of B, γ, and n are shown in Figure 3. Attempts to construct larger matrices generated software errors, and it was not judged necessary to try to pursue more complex calculations. Beyond $n = 73$, energies are approximated by assuming a power-law convergence towards the harmonic limit, i.e., $E_n - E_{n-2} - 2h\nu_{harmonic} \propto n^{-3/2}$ (Fig. S1). Separate convergence power-laws were used for even and odd n. To explore the effects of the size and width of the central potential peak, reduced partition function ratios and mass fractionation exponents are calculated on a grid of varying B, γ, and $h\nu_{harmonic}/k_BT$, where k_B is Boltzmann's constant and T is the absolute temperature. Numerical precision was generally worst at the highest temperatures ($h\nu_{harmonic}/k_BT \ll 1$), and with very localized Gaussian perturbations ($\gamma \gg 1$). However, the impact of these imprecisions is likely rather limited for two reasons.

1. Fractionations become very small at high temperatures and all mass fractionation laws should approach the harmonic high-T limit at these conditions, providing an analytic benchmark for determining numerical accuracy.

2. Highly localized Gaussians barriers are probably not physically realistic, as they are much sharper than the minima they separate. For example, the inversion mode in ammonia (NH_3), one of the simplest and best studied examples of a double-well potential, is fit well with $\gamma B \approx 0.9$–2.2 (Lin et al. 2007: $\gamma \approx 0.05$, $B \approx 17$; Earl 2008: $\gamma \approx 0.3$, $B \approx 8$), corresponding to a broad, large Gaussian perturbation.

Reconnaissance vibrational frequency calculations on the gas-phase $H_6Si_2O_7$ molecule in its ground-state bent conformation, compared to a strained configuration with the Si–O–Si angle fixed at 180°, suggest that γB for the Si–O–Si bending coordinate is also of order unity, with $B \gg 1$ and $\gamma \ll 1$. In particular, the similar absolute value of the force constants associated with the imaginary modes in "straight" Si–O–Si ($\nu_{bend} \approx 50i$ cm^{-1}), relative to the force constants of Si–O–Si bending in the relaxed, bent molecule ($\nu_{bend} \approx 60$–100 cm^{-1}), constrains $\gamma B \leq \sim 2$, while the large energy barrier (> 1000 cm^{-1}) between the relaxed and straight configurations indicates $B \geq \sim 10$, and thus $\gamma \leq \sim 0.2$. For the sake of simplicity, the calculations reported here assume $\nu_{harmonic}(^{16}O) = 200$ cm^{-1}. This corresponds roughly to the frequency of the soft-mode Si–O–Si vibrational frequency in α-quartz measured by Raman spectroscopy (e.g., Castex and Maddon 1995) but it should be noted that the characteristic frequency of the energy minima in the perturbed potential will not be the same as the harmonic frequency of the unperturbed potential—they will also depend on γB. Harmonic frequencies of isotopically-substituted oscillators in the model are assumed to scale in proportion to the reciprocal of the square root of the oxygen isotopic mass, as is observed for the soft-mode Si–O–Si vibration in completely ^{18}O-substituted quartz (Sato and McMillan 1987). This model is crude in important respects, for instance it treats the bending vibrational mode of one bridging oxygen as completely isolated from all other vibrations in the structure. However, this model does explore a scenario of anharmonic behavior that is likely to affect many important silicate and aluminosilicate minerals to a greater or lesser degree.

The nuclear field shift effect. The nuclear field shift effect has long been studied in high-resolution atomic spectroscopy (e.g., King 1984). It results from interactions between electrons and the finite volume and sometimes distorted shapes of atomic nuclei. All else equal, an electron inside the volume occupied by the nuclear charge "feels" a weaker Coulomb attraction than it would at the same distance from an infinitesimal point nucleus, and the resulting binding energy and orbital shape change slightly. Typically, nuclei with more neutrons (i.e., heavier isotopes) take up a greater volume of space, and overlap with a larger proportion of the electron cloud, but the correlation between mass and volume is irregular for many elements, including Oxygen (e.g., Miska et al. 1979). The nuclear field shift has been proposed to explain non-mass dependent isotope effects in some elements with high atomic number (e.g., Bigeleisen 1996; Nomura et al. 1996; Schauble 2007, for U and Tl, respectively) as well as a number of moderate-atomic number elements (e.g., Fujii et al. 2009). Theoretical calculations generally indicate that this

effect is much smaller for low atomic number elements such as sulfur and (presumably) oxygen (Knyaezev and Myasoedov 2001; Schauble et al. 2007), but $\Delta^{17}O$ measurements at the per meg level of precision suggest that quantitative estimates are now needed to evaluate hypotheses about the relationship between the Earth and Moon (e.g., Young et al. 2016; Herwartz et al. 2017) and other subtle oxygen isotope signatures. We estimated the volume component of the nuclear field shift effect on oxygen isotope fractionation in silicates using the method of Schauble (2013). In this method, the effect of varying the nuclear charge radii of oxygen atoms on the electronic energies of a calibration set of small molecules is calculated using relativistic all-electron quantum mechanics. These results are compared to electron densities at oxygen nuclei in the same molecules determined by Density Functional Theory models based on the Projector Augmented Wave (DFT-PAW) method. The calibrated energy/electron density relationship can then be used to estimate nuclear volume isotope effects with DFT-PAW models of crystal structures that are too complex to be directly modeled by the relativistic all-electron method.

Relativistic all-electron models use a high-accuracy electronic structure method, the coupled-cluster technique CCSD(T), including single and double excitations and a perturbative estimate of triple excitations, combined with the cc-pVTZ family of basis sets (Dunning 1989). Test calculations show little difference between field shift effects determined with this basis set, relative to the larger (and likely more accurate) aug-cc-pVTZ and cc-pVQZ basis sets, indicating that cc-pVTZ is accurate enough for the present purpose. In fact, the CCSD(T) energy differences are closely approximated by computationally simpler Dirac–Fock models, as was found previously in studies of higher atomic number elements (Cd, Sn, and Hg; Schauble 2013). Relativistic all-electron calculations were performed using the DIRAC15 code (Jensen et al. 2015).

There appears to be substantial uncertainty in experimental determinations of nuclear charge radii of the stable oxygen isotopes. For the present purpose, $^{18}O/^{16}O$ and $^{17}O/^{16}O$ field shift effects on relativistic CCSD(T) energies are calculated using the radii tabulated by Angeli and Marinova (2013) (2.6991 fm, 2.6932 fm, and 2.7726 fm for ^{16}O, ^{17}O, and ^{18}O respectively). Alternative radii determined by Singhal et al. (1970) and Miska et al. (1979) have also been considered. The Miska et al. (1979) results closely agree with Angeli and Marinova (2013), but Singhal et al. (1970) find a ~25–30% smaller difference in mean squared radii between ^{18}O and ^{16}O. However, all of these sets of radii yield very similar deviations from typical mass-fractionation exponents (i.e., disagreements in radii largely cancel so that any calculated $\Delta^{17}O$ is less sensitive to the choice of a radius reference).

DFT-PAW models are constructed mainly using version 1.0 of the JTH set of PAW data (Jollet et al. 2014), which is a publicly available library covering most of the periodic table that is similar in many respects to the GBRV and PSLibrary repositories described earlier. The JTH set has the advantage of being easier to set up for automatic computation of electron densities at the nuclei of oxygen atoms. A slightly modified PAW data set for O is used, with a shortened cut-off radius of 1.3 a_0 (0.69Å) and a finite-radius nucleus, as well as short cut-off radii PAW datasets for hydrogen and carbon (1.0 $a_0 \approx 0.53$ Å) from an older (pre-2013) public library associated with the AtomPAW project (see http://users.wfu.edu/natalie/papers/pwpaw/periodictable/oldperiodictable.html; Holzwarth et al. 2001). These short-cutoff PAW datasets are chosen to provide realistic results for molecular species with short bonds, including H_2O, CO, and CO_2, because PAW calculations generally work best when interatomic distances are at least as large as the sum of PAW cutoff radii. All DFT-PAW calculations used plane-wave basis sets with a kinetic energy cutoff of 60 Hartree (1633 eV). The models also all have periodic boundary conditions: crystal structures are modeled in experimentally determined periodic unit cells, and molecules are isolated individually in cubic or rectangular-prismatic cells that are at least 20 Bohr radii (10.3 Å) on a side to approximate the *in vacuo* condition of the corresponding relativisitic all-electron models.

Deviations from the Born–Oppenheimer approximation of electronic structure. Typically, electronic structure models of molecules and crystals adopt the Born–Oppenheimer approximation, which assumes that the motions of electrons and nuclei can be treated separately because nuclei are much more massive (and slower-moving) than electrons (Born and Oppenheimer 1927). A consequence of this assumption is that electronic energies are insensitive to the masses of isotopes, and equilibrium mass-dependent isotope effects arise only from the quantization of nuclear motion. However, in more accurate quantum-mechanical treatments nuclear masses do influence the coupled nuclear/electronic structure and energy in a way that is not captured by the Born–Oppenheimer approximation (e.g., Kleinman and Wolfsberg 1973; Bigeleisen 1996).

Zhang and Liu (2018) made a comprehensive examination of effects beyond the harmonic, Born–Oppenheimer approximation on equilibrium isotope fractionation, including an adaptation of the Born & Huang (1956) perturbative Diagonal Born–Oppenheimer Correction (DBOC) to account for nuclear/electronic coupling. They find that non-Born–Oppenheimer corrections are important for H/D substitution in molecules, and can even be significant (if much smaller) for isotope substitutions of heavier elements such as $^{13}C/^{12}C$ and $^{18}O/^{16}O$. For instance, in the $^{18}O/^{16}O$ fractionation between CO_2 and $H_2O(v)$, they find a DBOC correction of ~1‰ at 300 K, very similar in magnitude to the ~1‰ anharmonic ZPE correction described in the preceding section.

Although Zhang and Liu (2018) do not directly address possible $\Delta'^{17}O$ signatures arising from Born–Oppenheimer corrections, subsequent work (Cao et al. 2019; personal communication) indicates that the effects are very small (~1 ppm) at igneous temperatures, but may be more significant (several ppm) at ambient conditions. We have not included DBOC corrections into the results tabulated in this chapter, and this is an area where uncertainty remains.

How important are effects beyond the harmonic approximation?

Nuclear field shift fractionation. Calculated nuclear field shift fractionations are shown in Table 2. Because the nuclear charge radius of ^{17}O is similar to (or even smaller than) the charge radius of ^{16}O, while the radius of ^{18}O is larger, field shift effects on $\Delta'^{17}O$ are anti-correlated with (and somewhat smaller than) field shift $^{18}O/^{16}O$ fractionation. The range of estimated field shift fractionations is quite small, among O^{2-} species the largest fractionations are approximately 2 per meg in $^{18/16}\alpha$ and 1 per meg in $\Delta'^{17}O$ relative to a reference 0.528 mass fractionation exponent at 25 °C. The field shift will tend to increase $^{18}O/^{16}O$ in oxides, particularly silicates, because these species have the smallest electron densities at the oxygen nucleus. Higher oxidation states, including O^- in hydrogen peroxide, O^0 in dioxygen, and O^{2+} in F_2O, are predicted to be progressively depleted in ^{18}O, with positive field-shift induced $\Delta'^{17}O$. Nuclear field shift contributions to apparent $\Delta'^{17}O$ in inter-mineral fractionation among silicates (or for silicates relative to H_2O) are predicted to be very small (< 1 per meg) at all temperatures above 0 °C, relative to a $\theta = 0.528$ reference exponent. F_2O, containing oxygen in the 2+ oxidation state, is predicted to somewhat more strongly fractionated by the field shift effect relative to oxide and silicate species. These fractionations are expected to scale as $1/T$, and thus to be only ~1/3 to 1/6 as large (~0.1 per meg or less) in igneous and metamorphic rocks at near-solidus temperatures as they are at room temperature. Overall, field shift effects on both $^{18}O/^{16}O$ and $^{17}O/^{16}O$ fractionation appear to be so small that they are not considered further in this chapter. However, they may need to be taken into account if the accuracy of future analytical studies improves significantly beyond ±1 per meg level.

Anharmonic double-well potential. Representative results for the reduced partition function ratio $10^3 \ln^{18/16}\beta$ and the exponent $\theta_{a-atoms}$ are given in Table 3. In general, this type of potential does not appear to generate large deviations from typical mass-dependence for plausible values of the potential parameters. Models with $B = 10–20$ and $\gamma = 0.1$, which may roughly approximate Si–O–Si bending modes in polymerized silicates such as $H_6Si_2O_7(v)$ and

Table 2. Calculated $^{18}O/^{16}O$ and $^{17}O/^{16}O$ nuclear field shift fractionations, based on DFT-PAW electronic structure models calibrated against all-electron relativistic CCSD(T)/cc-pVTZ estimates of the nuclear volume effect on electronic energies.

Nuclear field shift effect in oxygen			$10^6 \ln^{18/16}\alpha(\text{X}-\text{H}_2\text{O})$		$\Delta'^{17}O$ vs. 0.528 (per meg)	
	Oxidation State	$\|\Psi(0)\|^2$ (e^-/a_0^3)	298 K	1000 K	298 K	1000 K
			Molecules			
OF_2	2	16.9	−4.1	−1.2	2.5	0.7
O_2	0	16.2	−2.6	−0.8	1.6	0.5
H_2O	−2	15.1	–	–	–	–
CO_2	−2	15.7	−1.3	−0.4	0.8	0.2
CO	−2	15.9	−1.9	−0.6	1.2	0.3
			Crystal Structures			
SiO_2 α-quartz	−2	14.7	0.8	0.2	−0.5	−0.2
$KAlSi_3O_8$ microcline	−2	14.8	0.7	0.2	−0.4	−0.1
$CaAl_2Si_2O_8$ anorthite	−2	14.8	0.6	0.2	−0.4	−0.1
$CaMgSi_2O_6$ diopside	−2	14.9	0.4	0.1	−0.3	−0.1
Mg_2SiO_4 forsterite	−2	14.9	0.3	0.1	−0.2	−0.1
H_4SiO_4	−2	14.9	0.3	0.1	−0.2	−0.1
$CaCO_3$ calcite	−2	15.1	0.0	0.0	0.0	0.0

Table 3. Mass dependence of oxygen isotope fractionation in a double-well potential in the form of a harmonic potential with a central Gaussian peak. Each entry gives $\Delta'^{17}O$ (in per meg) resulting from a single vibrational mode, consisting only of movement of an oxygen atom, relative to a $\theta = 0.528$ reference exponent. The shape of the central peak is described by its height (B) and sharpness (γ). B = 0 corresponds to an unperturbed harmonic potential. For a harmonic potential with a characteristic frequency of 200 cm^{-1}, $h\nu_{harm}/kT = 0.2$, 0.5, and 1 corresponds to $T = 288$ K, 576 K, and 1439 K, respectively. $B \approx 10$, $\gamma \approx 0.1$ may be a reasonable approximation for the Si–O–Si bending mode in $H_6Si_2O_7$. $B \approx 5$, $\gamma \approx 1$ (italics) may not be chemically reasonable for normal chemical bonding systems.

		$h\nu_{harmonic}/kT$		
B	γ	1	0.5	0.2
0 (harmonic)		10.5	2.8	0.5
1	1	6.7	2.5	0.5
2	1	0.9	2.3	0.5
5	1	−2.8	*3.0*	*0.6*
5	0.1	5.3	1.8	0.4
10	0.1	6.3	2.1	0.4
20	0.1	19.1	5.7	0.7

room-temperature α-quartz, show $\theta_{a-atoms}$ between 0.529 and 0.531 at temperatures above 273 K, and are within 0.001 of the pure harmonic 200 cm^{-1} oscillator. Because this is above the reference exponent of 0.528, the effect of these vibrational modes will be to slightly increase $\Delta'^{17}O$ in polymerized species, relative to other substances. $10^3 \ln^{18/16}\beta$ is more variable within this range of potential parameters, from ~4‰ at 288 K for $B = 10$ to ~11‰ at $B = 20$. This can be rationalized as reflecting the increase in the curvature of the potential at the energy minima as B increases, leading to a larger effective force constant, and would be accompanied by a larger measured fundamental vibrational frequency. Relative to a 0.528 reference exponent, $10^3 \ln^{18/16}\beta$ and $10^3 \ln^{18/16}\beta$ for the $B = 10$, $\gamma = 0.1$ potential would yield $\Delta'^{17}O = +6$ per meg at 288 K and +0.4 per meg at 1439 K; the $B = 20$, $\gamma = 0.1$ potential would yield $\Delta'^{17}O = +19$ per meg at 288 K and +0.7 per meg at 1439 K. For comparison, a pure harmonic oscillator at 200 cm^{-1} yields $\Delta'^{17}O = +10$ per meg at 288 K, and +0.5 per meg at 1439 K. In fact, no combination of parameters with $B\gamma \leq 2$, $B \leq 20$ appears to generate $\Delta'^{17}O$ signatures ≥ 10 per mg at ambient temperatures (~300 K), or ≥ 1–2 per meg at temperatures above 1000 K. Potentials with larger $B\gamma$ can (Fig. 4), especially at low temperatures and at large B, but this parameter range may not be relevant to normal natural materials. Note that the parameter sampling used to generate this contour plot is rather coarse and certainly is not exhaustive, so interpolated variations should be taken as a rough guide. It should also be noted that a perturbed harmonic potential is only one of many possible, chemically plausible double-well and multiple-well potentials. Other realistic variants could conceivably generate larger signatures at temperatures of interest.

In summary, these reconnaissance calculations appear to show that at least one form of double-well anharmonicity can generate $\Delta'^{17}O$ signatures of order ±10 per meg at near-ambient or hydrothermal temperatures, and thus may be useful to consider as a correction to harmonic estimates in future high-precision theoretical studies of polymerized silicates, hydrogen bonded materials such as liquid water, ice, and organic matter. However, it is unlikely to explain the negative $\Delta'^{17}O$ observed in polymerized silicate minerals fractionated at high temperatures (Sharp et al. 2016; Young et al. 2016) for two reasons. First, the effect appears to be too small (< 1 per meg at $T > 1200$ K), and second, the calculated effects have the opposite sign to observed signatures (> 0 for the model potential, vs. < 0 in measured granite and feldspars). Anharmonic effects on the mass fractionation exponent will be ignored in the discussion that follows, excepting the anharmonic zero-point energy correction previously described for $H_2O(v)$, CO_2, and CO.

$\Delta'^{17}O$ signatures of equilibrium

Based on the discussion and findings above, it appears likely that mass-dependent effects within the Born–Oppenheimer approximation are usually the predominant driver of $\Delta'^{17}O$ at equilibrium, including at high (metamorphic and igneous) temperatures, and that even simplified calculations based on these assumptions can generate reasonable estimates of signatures found in natural systems. Newly calculated mass dependent $10^3 \ln^{18/16}\beta$ and $\theta_{a-atoms}$ results from the present work are reported in Table 4. Polynomials in $1/T$ have been fit to each, in order to facilitate interpolation (Tables 5 and 6) for temperatures above 243.15 K. Fits for $10^3 \ln^{18/16}\beta$ are accurate to within 0.03‰, and fits for $\theta_{a-atoms}$ are accurate within 1×10^{-4} over this temperature range. Model properties for liquid and supercritical water are also tabulated (273.15–647 K for liquid water and 647+ K for supercritical water), by adding $10^3 \ln^{18/16}\alpha$ for liquid–vapor or supercritical fluid–vapor (Horita and Wesolowski 1994; Rosenbaum 1997) to the present H_2O vapor results. $\theta_{liquid\ water-atoms}$ is estimated as described above.

Uncertainties in estimated mass-dependent fractionations. Leaving aside anharmonicity, which has been addressed in a special case above, more generally by Richet et al. (1977), Schauble et al. (2006) Méheut et al. (2007), and others for the calculation of stable isotope fractionation factors, and in greater detail by Cao and Liu (2011) for estimating θ_{a-b} exponents, the main contributors to uncertainty in estimated $^{18}O/^{16}O$ and θ_{a-b} are likely to be errors in calculated
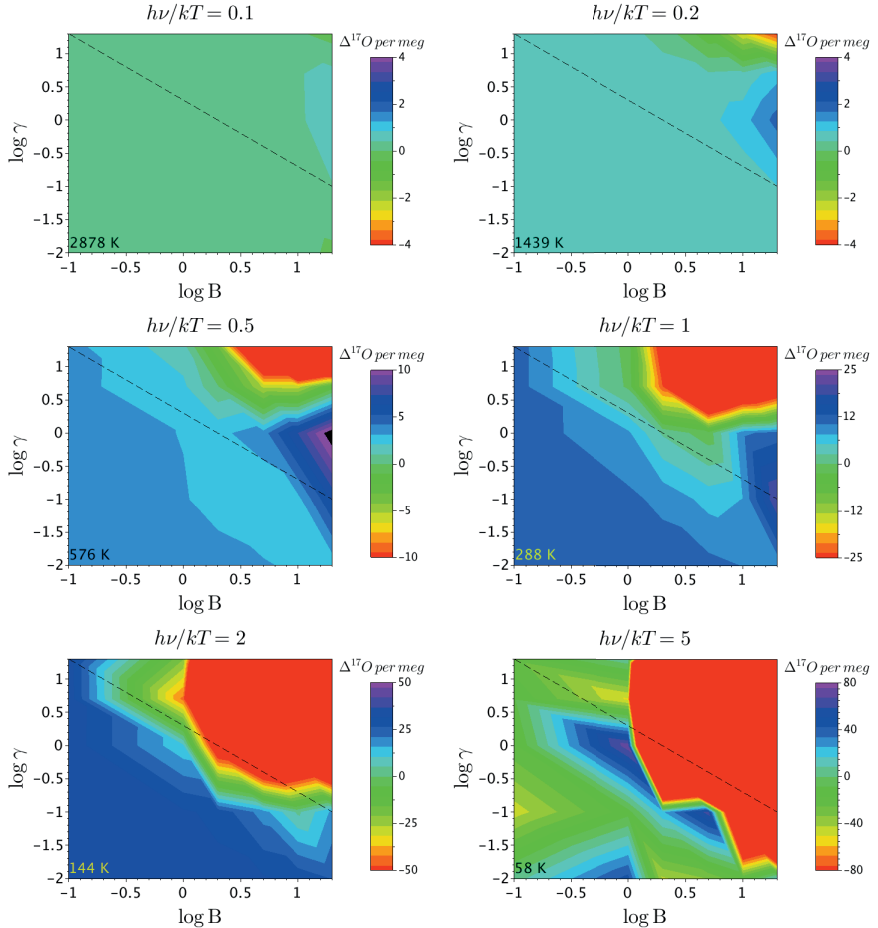
Figure 4. Contour plots showing variation in the calculated $\Delta'^{17}O$ (in per meg), relative to a $\theta = 0.528$ reference exponent, for an anharmonic oscillator in a double-well potential, versus the height (B) and sharpness (γ) of the central Gaussian. Temperatures are given for each panel, based on the assumption that the harmonic component of the potential has a characteristic frequency of 200 cm^{-1}. The corresponding $\Delta'^{17}O$ for the unperturbed harmonic potential is shown with a **white line** labelled "B = 0" in each color scalebar. The dashed black line indicates $B\gamma = 2$; it is likely that silicates and other molecules with double-well potentials are best fit by values of B and γ that fall below this line.

vibrational frequencies, errors in the frequency shifts upon isotope substitution, errors from incomplete sampling of the phonon density of states, and errors stemming from the interaction of ^{18}O or ^{17}O substitutions in adjacent unit cells. We will attempt to address each of these sources of error in turn, though it is still not possible to provide a rigorous quantitative analysis.

    Scale factor effects. Application of a frequency scale factor is intended to correct for the typical systematic error in the PBE gradient-corrected approximation of the density functional. This work and many previous studies have found consistent underestimation of both measured and harmonic frequencies, by ~3–6% in materials most closely resembling the crystals studied here. However, there are still potentially significant mismatches between measured and calculated frequencies even when the scale factor is applied. One approach to estimating this source of uncertainty is to compare our results with a general fitted PBE scale factor

Table 4. Calculated 1000 ln$^{18/16}$β, θ$_{a-atoms}$, and Δ'^{17}O (vs. H$_2$O vapor) for crystals and molecules at 0°C (273.15 K), 25°C (298.15 K), and 100°C (373.15 K). Anharmonic zero-point energy corrections are included in estimated ln$^{18/16}$β for H$_2$O vapor (anharm.), CO, and CO$_2$. θ$_{a-atoms}$ is based on harmonic oscillator models for all species. Liquid water results are based on both anharmonic and harmonic H$_2$O vapor models, and assume the liquid–vapor fractionation of Rosenbaum (1997; R-model) and Horita and Wesolowski (1994; HW-model). θ$_{a-atoms}$ for the liquid water results shown here are calculated as the average of H$_2$O vapor and ice-Ih.

Substance	1000 ln$^{18/16}$β			θ$_{a-atoms}$			Δ'^{17}O vs. H$_2$O vapor (per meg)		
	0°C	25°C	100°C	0°C	25°C	100°C	0°C	25°C	100°C
α-quartz	124.83	108.70	75.20	0.527906	0.528118	0.528653	−149.6	−112.4	−48.4
Albite (low)	117.11	101.69	69.85	0.528103	0.528315	0.528835	−125.9	−93.2	−39.2
Microcline (low)	116.71	101.36	69.67	0.528091	0.528304	0.528827	−127.2	−94.4	−39.9
Anorthite (ordered)	109.91	95.18	64.97	0.528301	0.528509	0.529005	−104.8	−76.8	−32.2
Diopside	104.55	90.30	61.26	0.528508	0.528708	0.529177	−84.8	−61.3	−25.4
Jadeite	112.83	97.57	66.37	0.528331	0.528540	0.529037	−100.6	−72.5	−28.6
Forsterite	99.47	85.60	57.59	0.528764	0.528955	0.529387	−61.9	−43.5	−17.6
Zircon	103.09	88.98	60.26	0.528501	0.528705	0.529180	−86.3	−62.5	−26.4
Grossular	100.67	86.55	58.10	0.528798	0.528991	0.529421	−57.5	−39.5	−14.9
Lizardite	99.51	86.28	59.37	0.528679	0.528875	0.529320	−70.3	−49.8	−19.1
Kaolinite	111.96	97.25	67.12	0.528556	0.528750	0.529201	−75.7	−52.3	−16.9
Phlogopite	103.73	89.72	61.19	0.528512	0.528718	0.529194	−84.8	−60.9	−24.4
Tremolite	107.42	92.96	63.41	0.528349	0.528561	0.529062	−100.4	−73.1	−30.1
Glaucophane	111.51	96.57	65.98	0.528261	0.528476	0.528989	−108.8	−79.3	−32.2
Spinel (normal)	96.70	82.79	55.02	0.529026	0.529214	0.529615	−38.6	−24.7	−8.6
Diaspore	105.10	90.65	61.53	0.529025	0.529193	0.529552	−30.1	−17.1	−2.0
Xenotime YPO$_4$	108.35	93.74	63.85	0.528427	0.528627	0.529103	−91.6	−66.4	−27.1
Xenotime LuPO$_4$	110.20	95.35	64.97	0.528401	0.528603	0.529083	−93.7	−67.8	−27.1
Monazite LaPO$_4$	103.09	89.19	60.75	0.528464	0.528660	0.529127	−90.0	−66.4	−29.0

Substance	1000 ln$^{18/16}\beta$			$\theta_{\alpha-atoms}$			Δ^{17}O vs. H$_2$O vapor (per meg)		
	0°C	25°C	100°C	0°C	25°C	100°C	0°C	25°C	100°C
Fluorapatite	104.31	90.29	61.57	0.528453	0.528649	0.529115	−90.6	−66.7	−28.8
Anhydrite	111.93	97.16	66.71	0.528319	0.528515	0.528992	−102.1	−75.2	−31.3
Barite	107.41	93.19	63.89	0.528387	0.528578	0.529044	−96.3	−71.3	−30.8
Gypsum (all O)	102.18	89.34	62.71	0.528635	0.528833	0.529277	−73.0	−50.8	−17.4
Gypsum (sulfate O)	109.41	94.94	65.12	0.528366	0.528559	0.529029	−97.9	−72.2	−30.5
Gypsum (H$_2$O)	87.58	78.04	57.88	0.529769	0.529813	0.529912	10.3	9.9	8.1
NaClO$_4$	106.54	92.47	63.43	0.528392	0.528584	0.529052	−96.1	−71.2	−30.8
Calcite	114.44	99.75	69.22	0.528436	0.528609	0.529036	−88.0	−64.5	−25.7
Aragonite	113.69	99.16	68.91	0.528421	0.528592	0.529017	−90.0	−66.5	−27.4
Dolomite	119.53	104.15	72.22	0.528414	0.528590	0.529022	−88.4	−63.8	−23.7
Magnesite	124.82	108.68	75.26	0.528409	0.528587	0.529023	−86.8	−61.4	−20.5
Nahcolite	121.52	106.37	74.67	0.528435	0.528600	0.529009	−85.1	−61.5	−22.1
Nitratine	111.71	97.52	67.85	0.528406	0.528579	0.529013	−92.5	−68.7	−28.8
H$_2$O vapor (anharm.)	68.29	61.70	47.26	0.530019	0.530030	0.530063	0	0	0
H$_2$O vapor (harm.)	71.68	64.81	49.74	0.530018	0.530029	0.530062	0	0	0
Liquid water (R-model, anharm.)	79.81	70.65	52.11	0.529889	0.529918	0.529988	12.9	10.3	6.1
Liquid water (R-model, harm.)	83.20	73.75	54.59	0.529889	0.529918	0.529988	–	–	–
Liquid water (HW-model, anharm.)	80.04	71.01	52.34	0.529889	0.529918	0.529988	13.3	11.0	6.6
Liquid water HW-model, harm.)	83.43	74.11	54.82	0.529889	0.529918	0.529988	–	–	
Water Ice Ih (harm.)	91.31	81.04	59.42	0.529760	0.529807	0.529915	16.1	14.9	11.2
Water Ice XI (harm.)	91.39	81.11	59.48	0.529760	0.529806	0.529914	16.1	15.0	11.3
CO$_2$ vapor (anharm.)	123.57	109.54	79.39	0.527852	0.527985	0.528366	−156.2	−126.8	−68.4
CO vapor (anharm.)	112.84	101.33	76.10	0.528128	0.528201	0.528429	−123.4	−104.8	−64.9
H$_4$SiO$_4$ vapor	100.53	88.19	62.54	0.529053	0.529192	0.529509	−32.0	−20.2	−3.1

Table 5. Polynomial fits of the form $1000 \ln^{18/16}\beta = A/T^6 + B/T^5 + C/T^4 + D/T^3 + E/T^2 + F/T$ for temperatures above 243.15 K (273.15 K for liquid water). A temperature independent term, "G", is included in the fits for liquid water, taken directly from earlier liquid–vapor and supercritical fluid–vapor studies (Rosenbaum 1997; Horita and Wesolowski 1994).

Substance	$1000 \ln^{18/16}\beta$			$\theta_{a-atoms}$			$\Delta^{17}O$ vs. H_2O vapor (per meg)		
	0°C	25°C	100°C	0°C	25°C	100°C	0°C	25°C	100°C
$H_6Si_2O_7$ vapor bridging O	126.57	109.86	75.38	0.528221	0.528429	0.528935	−109.9	−78.1	−27.0

Substance	A	B	C	D	E	F	G
α-quartz	−8.57662E+15	1.29277E+14	−6.47264E+11	1.13149E+08	1.27764E+07	−1.58089E+01	–
Albite (low)	−6.38987E+15	1.00579E+14	−5.33809E+11	1.54282E+08	1.15385E+07	6.24956E+00	–
Microcline (low)	−6.46928E+15	1.01670E+14	−5.38345E+11	1.56396E+08	1.15223E+07	6.38887E+00	–
Anorthite (ordered)	−4.67984E+15	7.71919E+13	−4.34289E+11	1.57751E+08	1.04922E+07	1.60620E+01	–
Diopside	−3.62416E+15	6.16464E+13	−3.60713E+11	1.44442E+08	9.72754E+06	1.80991E+01	–
Jadeite	−4.40482E+15	7.31080E+13	−4.15958E+11	1.52614E+08	1.06345E+07	1.60881E+01	–
Forsterite	−2.19103E+15	4.08989E+13	−2.65461E+11	1.19351E+08	8.92416E+06	1.89238E+01	–
Zircon	−3.23144E+15	5.63538E+13	−3.38586E+11	1.45392E+08	9.50742E+06	2.04146E+01	–
Grossular	−1.88297E+15	3.66292E+13	−2.47596E+11	1.14579E+08	8.94561E+06	1.92367E+01	–
Lizardite	7.73661E+15	−1.12366E+14	6.86921E+11	−2.81599E+09	1.26740E+07	−8.49823E+01	–
Kaolinite	6.51056E+15	−9.35842E+13	5.89200E+11	−2.76100E+09	1.40130E+07	−9.49342E+01	–
Phlogopite	7.27276E+14	−4.55563E+12	3.47214E+10	−9.73368E+08	1.09344E+07	−1.45729E+01	–
Tremolite	−2.12065E+15	3.79732E+13	−2.04889E+11	−4.08901E+08	1.07765E+07	−2.36835E+00	–
Glaucophane	−2.63255E+15	4.51509E+13	−2.37314E+11	−4.08262E+08	1.12546E+07	−6.21183E+00	–
Spinel (normal)	−6.18560E+14	1.71233E+13	−1.51621E+11	6.83972E+07	8.26379E+06	1.35275E+01	–
Diaspore	4.57904E+15	−7.03550E+13	4.54600E+11	−2.10919E+09	1.21732E+07	−2.67567E+02	–
Xenotime YPO₄	−4.39155E+15	7.26398E+13	−4.11008E+11	1.51631E+08	1.02582E+07	1.59587E+01	–
Xenotime LuPO₄	−4.56891E+15	7.51877E+13	−4.22893E+11	1.52834E+08	1.04575E+07	1.53390E+01	–

Substance	A	B	C	D	E	F	G
Monazite LaPO$_4$	−4.13682E+15	6.87433E+13	−3.90816E+11	1.47530E+08	9.75493E+06	1.62466E+01	–
Fluorapatite	−4.37161E+15	7.20071E+13	−4.05288E+11	1.47629E+08	9.92196E+06	1.50223E+01	–
Anhydrite	−5.96338E+15	9.37217E+13	−4.97617E+11	1.29805E+08	1.10175E+07	2.01074E+00	–
Barite	−5.39636E+15	8.58034E+13	−4.62533E+11	1.30922E+08	1.04920E+07	5.27267E+00	–
Gypsum (all O)	8.03873E+15	−1.25014E+14	8.53232E+11	−3.81657E+09	1.49278E+07	−2.81301E+02	–
Gypsum (sulfate O)	−5.50349E+15	8.73493E+13	−4.68492E+11	1.13100E+08	1.07298E+07	3.79932E+00	–
Gypsum (H$_2$O)	3.50923E+16	−5.48078E+14	3.47959E+12	−1.16216E+10	2.32601E+07	−8.30661E+02	–
NaClO$_4$	−5.30560E+15	8.48246E+13	−4.60322E+11	1.34434E+08	1.04159E+07	6.62368E+00	–
Calcite	−8.13464E+15	1.16592E+14	−5.39168E+11	−1.93699E+08	1.22391E+07	−8.98300E+01	–
Aragonite	−8.31575E+15	1.18153E+14	−5.37818E+11	−2.40930E+08	1.22970E+07	−1.02204E+02	–
Dolomite	−8.39772E+15	1.19880E+14	−5.50664E+11	−2.25445E+08	1.27776E+07	−9.88440E+01	–
Magnesite	−8.52650E+15	1.21467E+14	−5.56075E+11	−2.53019E+08	1.32925E+07	−1.06063E+02	–
Nahcolite	−6.36640E+15	7.90625E+13	−2.20150E+11	−1.56554E+09	1.51029E+07	−3.28073E+02	–
Nitratine	−8.18521E+15	1.19422E+14	−5.67548E+11	−1.04293E+08	1.19529E+07	−6.82541E+01	–
H$_2$O vapor (anharm.)	4.08073E+16	−6.26044E+14	3.88795E+12	−1.25885E+10	2.28002E+07	−1.24437E+03	–
H$_2$O vapor (harm.)	4.15943E+16	−6.37102E+14	3.94849E+12	−1.27503E+10	2.30136E+07	−4.32931E+02	–
Water Ice Ih	2.55981E+16	−4.14442E+14	2.75605E+12	−9.81791E+09	2.18496E+07	−1.07955E+03	–
Water Ice XI	2.56214E+16	−4.14778E+14	2.75816E+12	−9.82552E+09	2.18670E+07	−1.07882E+03	–
CO$_2$ vapor	−6.27638E+15	4.56379E+13	2.68853E+11	−4.27840E+09	2.05286E+07	−1.32159E+03	–
CO vapor	−1.93531E+15	−6.95760E+13	1.31394E+12	−8.38839E+09	2.58267E+07	−2.00113E+03	–
H$_4$SiO$_4$ vapor	2.09683E+16	−3.10907E+14	1.88036E+12	−6.45554E+09	1.74651E+07	−1.60791E+02	–
H$_6$Si$_2$O$_7$ vapor bridging O	−6.23677E+15	1.00933E+14	−5.54067E+11	1.87949E+08	1.23447E+07	1.63985E+01	–

Stums of $10^3 ln\beta$ H_2O vapor and $10^3 ln\alpha$ H_2O liquid-vapor or $10^3 ln\alpha$ H_2O supercritical-vapor from Rosenbaum (1997)

Liquid Water (anharm.) (273–403 K)	2.86501E+15	−6.66957E+12	−8.59748E+10	−1.15346E+08	6.40332E+06	−6.46500E+01	12.815
Liquid Water (anharm.) (403–647 K)	1.20346E+17	−6.66957E+12	−1.98057E+12	−1.15346E+08	1.67523E+07	−6.46500E+01	−6.482

Substance	A	B	C	D	E	F	G
Supercritical Water (anharm.) (≥ 647 K)	5.58246E+17	-6.66957E+12	-2.77257E+12	-1.15346E+08	1.29963E+07	-6.46500E+01	–
Liquid Water (harm.) (273–403 K)	3.65207E+15	-1.77280E+13	-2.54358E+10	-2.77134E+08	6.61672E+06	7.46789E+02	12.815
Liquid Water (harm.) (403–647 K)	1.21133E+17	-1.77280E+13	-1.92004E+12	-2.77134E+08	1.69657E+07	7.46789E+02	-6.482
Supercritical Water (harm.) (≥ 647 K)	5.59033E+17	-1.77280E+13	-2.71204E+12	-2.77134E+08	1.32097E+07	7.46789E+02	–
Sums of $10^3 \ln \beta$ H_2O vapor and $10^3 \ln \alpha$ H_2O liquid–vapor from Horita and Wesolowski (1994)							
Liquid Water (anharm.) (273–647 K)	4.08073E+16	-6.26044E+14	3.88795E+12	-1.22381E+10	2.11338E+07	5.46793E+03	-7.685
Liquid Water (harm.) (273–647 K)	4.15943E+16	-6.37102E+14	3.94849E+12	-1.23999E+10	2.13472E+07	6.27937E+03	-7.685
Fits to results of Rosenbaum (1997), used to estimate properties of liquid and supercritical water							
H_2O vapor	4.03612E+16	-6.19374E+14	3.84852E+12	-1.24732E+10	2.26339E+07	-1.17972E+03	–
$10^3 \ln \alpha$ H_2O liquid–vapor (273–403K)	-3.79422E+16	6.19374E+14	-3.97392E+12	1.24732E+10	-1.63969E+07	1.17972E+03	12.815
$10^3 \ln \alpha$ H_2O liquid–vapor (403–647K)	7.95388E+16	6.19374E+14	-5.86852E+12	1.24732E+10	-6.04789E+06	1.17972E+03	-6.482
$10^3 \ln \alpha$ H_2O supercritical–vapor (≥ 647K)	5.17439E+17	6.19374E+14	-6.66052E+12	1.24732E+10	-9.80389E+06	1.17972E+03	–

Table 6. Polynomial fits of the form $\theta_{a-atoms} = 0.530520 + L/T^4 + M/T^3 + N/T^2 + P/T$ for temperatures above 243.15 K (273.15 K for liquid water).

Substance	L	M	N	P
α–quartz	-9.84260E+06	1.34471E+05	-5.72152E+02	6.08257E-02
Albite (low)	-7.15131E+06	1.05390E+05	-4.84222E+02	5.02774E-02
Microcline (low)	-7.07921E+06	1.05174E+05	-4.85387E+02	5.07437E-02
Anorthite (ordered)	-5.22563E+06	8.32484E+04	-4.11634E+02	4.10861E-02
Diopside	-3.43390E+06	6.23164E+04	-3.41450E+02	3.30828E-02
Jadeite	-4.79241E+06	7.78984E+04	-3.95169E+02	3.92213E-02
Forsterite	-1.70288E+06	4.00637E+04	-2.61182E+02	2.26548E-02
Zircon	-3.01991E+06	5.85699E+04	-3.33492E+02	3.19019E-02

Substance	L	M	N	P
Grossular	-1.25214E+06	3.47731E+04	-2.44601E+02	2.01696E-02
Lizardite	6.78135E+05	1.79214E+04	-1.91993E+02	-7.41326E-02
Kaolinite	-1.82963E+06	4.21814E+04	-2.57960E+02	-6.81728E-02
Phlogopite	-1.31818E+06	4.19366E+04	-2.82492E+02	-1.24930E-02
Tremolite	-3.26905E+06	6.39611E+04	-3.58080E+02	2.02277E-02
Glaucophane	-4.22525E+06	7.44971E+04	-3.92412E+02	2.75325E-02
Spinel (normal)	2.11190E+05	1.43521E+04	-1.69555E+02	9.68832E-03
Diaspore	-3.20897E+06	3.77741E+04	-1.87320E+02	-7.02837E-02
Xenotime YPO_4	-4.36909E+06	7.30846E+04	-3.75570E+02	3.76112E-02
Xenotime $LuPO_4$	-4.56535E+06	7.53224E+04	-3.83345E+02	3.85453E-02
Monazite $LaPO_4$	-4.25029E+06	7.16694E+04	-3.69102E+02	3.70972E-02
Fluorapatite	-4.45849E+06	7.38756E+04	-3.75391E+02	3.78383E-02
Anhydrite	-6.29166E+06	9.36614E+04	-4.35133E+02	4.48193E-02
Barite	-5.82495E+06	8.81142E+04	-4.15417E+02	4.24829E-02
Gypsum (all O)	-1.71512E+05	1.82458E+04	-1.62159E+02	-1.57186E-01
Gypsum (sulfate O)	-5.87792E+06	8.89986E+04	-4.19591E+02	4.27316E-02
Gypsum (H_2O)	-6.87656E+06	5.60349E+04	-1.18337E+02	-1.82943E-01
$NaClO_4$	-5.49862E+06	8.53229E+04	-4.09047E+02	4.19470E-02
Calcite	-8.74242E+06	1.11775E+05	-4.58694E+02	4.10091E-02
Aragonite	-9.24375E+06	1.16665E+05	-4.71117E+02	4.15681E-02
Dolomite	-8.93017E+06	1.13330E+05	-4.63424E+02	4.06824E-02
Magnesite	-8.88665E+06	1.12414E+05	-4.60718E+02	3.95939E-02
Nahcolite	-1.05391E+07	1.24829E+05	-4.75553E+02	1.61644E-02
Nitratine	-8.48622E+06	1.11387E+05	-4.63752E+02	4.37314E-02
H_2O vapor (anharm.)	-5.55222E+06	4.16832E+04	-5.59908E+01	-2.15903E-01

Schauble & Young

Substance	L	M	N	P
H_2O vapor (harm.)	−5.44629E+06	4.05846E+04	−5.21169E+01	−2.20711E−01
Water Ice Ih	−7.55686E+06	6.38621E+04	−1.50800E+02	−1.38100E−01
Water Ice XI	−7.57522E+06	6.40300E+04	−1.51169E+02	−1.38290E−01
CO_2 vapor	−2.75388E+07	2.78083E+05	−8.40698E+02	−2.28591E−02
CO vapor	−3.93502E+07	3.58154E+05	−9.25062E+02	−1.27385E−01
H_4SiO_4 vapor	−2.33424E+06	3.28910E+04	−1.59882E+02	−1.40973E−01
$H_6Si_2O_7$ vapor bridging O	−5.84665E+06	9.14111E+04	−4.40417E+02	4.54413E−02
Liquid and Supercritical Water (anharm.; ≥ 273K) using $10^3 \ln \alpha\ H_2O$ liquid–vapor from Rosenbaum (1997)				
$\theta_{liquid–vapor}$ = 0.529 (Barkan et al. 2005)	−5.49858E+07	4.63855E+05	−1.22371E+03	7.87587E−01
Lesser of vapor vs. previous	−7.28054E+06	5.94857E+04	−1.22058E+02	−1.69771E−01
50% ice model	−8.79767E+06	6.73660E+04	−1.31127E+02	−1.62891E−01
Liquid and Supercritical Water (anharm.; ≥ 273K) using $10^3 \ln \alpha\ H_2O$ liquid–vapor from Rosenbaum (1997)				
$\theta_{liquid–vapor}$ = 0.529 (Barkan et al. 2005)	−4.99105E+07	4.21352E+05	−1.10973E+03	6.92261E−01
Lesser of vapor vs. previous	−7.26651E+06	5.89854E+04	−1.19406E+02	−1.71835E−01
50% ice model	−8.79767E+06	6.73660E+04	−1.31127E+02	−1.62891E−01
Liquid Water (anharm.; 273K ≤ T ≤ 647K) using $10^3 \ln \alpha\ H_2O$ liquid–vapor from Horita and Wesolowski (1994)				
$\theta_{liquid–vapor}$ = 0.529 (Barkan et al. 2005)	−1.25778E+07	1.08486E+05	−2.70736E+02	−2.28243E−02
Lesser of vapor vs. previous	−1.01415E+07	8.71902E+04	−2.10441E+02	−7.78492E−02
50% ice model	−1.24040E+06	6.01304E+03	2.66231E+01	−2.89380E−01
Liquid Water (harm.; 273K ≤ T ≤ 647K) using $10^3 \ln \alpha\ H_2O$ liquid–vapor from Horita and Wesolowski (1994)				
$\theta_{liquid–vapor}$ = 0.529 (Barkan et al. 2005)	−1.18765E+07	1.02119E+05	−2.51906E+02	−3.92103E−02
Lesser of vapor vs. previous	−9.58417E+06	8.20815E+04	−1.95176E+02	−9.09826E−02
50% ice model	−1.24040E+06	6.01304E+03	2.66231E+01	−2.89380E−01

to alternative calculations using separate, mineral specific or mineral-type specific scale factors, for instance applying a ~3% correction for carbonates, 4–5% for silicates, and ~5–6% for sulfates, phosphates, and perchlorates, based on correlations of subgroups of crystals with measured spectra reported in this study. As detailed by Meheut et al. (2007), the effects of such scale factor adjustments can be estimated using an effective power law scaling, e.g. $\ln\beta(SF_1)/\ln\beta(SF_2) = (SF_1/SF_2)^p$, where β are predicted $^{18}O/^{16}O$ reduced partition function ratios calculated by applying two different scale factors (SF_1 and SF_2) to a given set of modeled vibrational frequencies for some substance. The exponent p is expected to be slightly less than 2 for typical oxygen-bearing compounds at geochemically relevant temperatures. Alternatively, one can simply scale the temperature, because frequency and temperature always appear as a ratio in the calculation of a reduced partition function ratio; i.e., $\ln\beta(SF_1)$ at $T = T_1$ is equal to $\ln\beta(SF_2)$ at $T = T_1(SF_2/SF_1)$. Either way, one would expect that ~1% uncertainty or scatter in frequency scale factors will lead to ~2‰ scatter in $1000\ln^{18/16}\beta$, given typical values of ~80–110‰ for $1000\ln^{18/16}\beta$ at 300 K for many of the crystals in this study. Errors will be correspondingly smaller at high temperatures. This uncertainty is much larger than typical $^{18}O/^{16}O$ measurement precisions, and is likely to be a major source of potential error in the present calculations. However, the effect of scale factor uncertainty on calculated $\theta_{a-atoms}$ is much smaller. Test calculations with varying scale factors for α-quartz, diaspore, anhydrite, and calcite indicate a typical perturbation of ~2×10^{-5} on $\theta_{a-atoms}$ when the scale factor is varied by 1%, which is a precision well beyond current measurement capabilities. This result agrees with the scaling arguments presented by Cao and Liu (2011), suggesting that the mass law exponent will be a robust product of theoretical models in the absence of large errors in the electronic structure or major anharmonic effects. Uncertainties from residual random scatter in frequencies after scaling are expected to be even smaller due to partial cancellations of errors.

Another approach to estimating uncertainties stemming from using the PBE functional to calculate vibrational frequencies is to compare models using different electronic structure methods, in the expectation that both systematic and random errors will change as well. Comparisons with molecule-based and cluster models using hybrid density functional theory (e.g., B3LYP; Becke 1993) and higher-order methods such as Møller-Plesset theory (MP2; Møller and Plesset 1934) provide the most robust tests of this sort. The $\theta_{a-atoms}$ results of Cao and Liu (2011) and Haynes et al. (2018) using such methods are thus of particular value, and are discussed in detail in a later section. As an additional check, we created models of a subset of crystals (α-quartz, diaspore, anhydrite, calcite) and molecules (water vapor and carbon dioxide) using two different density functionals: the Local Density Approximation functional (as parameterized by Perdew and Zunger 1981), here abbreviated LDA, and the PBEsol gradient corrected density functional optimized for accurately reproducing lattice constants of solids (Perdew et al. 2007). Frequency scale factors are determined independently for the models using each functional, these are 3.8% for PBE (slightly different from the 4.3% scaling fitted to the whole PBE model suite), 1.6% for the LDA models, and 2.7% for the PBEsol models. The residual scatter after fitting the scale factors for the PBE and PBEsol models for these six substances is similar (rms misfit of 17 cm^{-1} vs. 16 cm^{-1} respectively). The rms frequency over the correlated modes is 962 cm^{-1}, suggesting slightly less than 2% relative scatter, which is similar to the larger set of correlated PBE models. The residual scatter for the LDA models is slightly larger (23 cm^{-1}). Calculated reduced partition function ratios and $\theta_{a-atoms}$ are shown in Table 7. The two gradient-corrected functionals show typical mismatches of ~1–2‰ at 300 K, consistent with the crude scale-factor based estimate above, but this test may be overly optimistic given the close theoretical relationship between PBE and PBEsol. The LDA models are more variable, with mismatches of up to 4‰. $\theta_{a-atoms}$ is much less sensitive to the choice of functional, varying by less than 5×10^{-5} between PBE and PBEsol models, and by less than 1×10^{-4} between PBE and LDA models.

Effects of sampling the phonon density of states. The potential effects of incomplete phonon sampling on reduced partition function ratios and isotopic clumping have been discussed previously (e.g., Elcombe and Hulston 1975; Schauble et al. 2003, 2006; Méheut et al. 2007). As in prior work, these effects are estimated in the present study by comparing models of a subset of crystals (α-quartz, diaspore, anhydrite, calcite, and aragonite) using a coarser phonon wave vector sampling (with roughly half as many distinct wave vectors). The test results are shown in Table 8. They show a limited dependence of $^{18}O/^{16}O$ fractionation, with less than 0.2‰ variation at 298.15 K in all cases. $\theta_{a-atoms}$ varies by no more than 5×10^{-5} in all cases. The lack of sensitivity of $\theta_{a-atoms}$ to phonon wave vector sampling suggests that adequate results can often be obtained on a sampling grid containing only one distinct wave vector, so long as it is chosen with care.

The variation in calculated reduced partition function ratios with fine vs. coarse phonon wave vector grids is notably smaller than the ~1‰ variation found in previous work on rhombohedral carbonates (Schauble et al. 2006) using phonon wave vector samples of similar size. An important difference in the earlier work is that in general only one atomic position per unit cell in each crystallographic site was included in the thermodynamic calculation, whereas the present study accounts for all oxygen atoms on each unit cell through a series of one-atom isotopic substitutions. This improves convergence because the crystallographic symmetries of a lattice are commonly split along the phonon wave vector, so that (for instance) ^{18}O substitution on one of the O(2) atomic positions in aragonite will not necessarily generate the same frequency shifts for a particular phonon wave vector as ^{18}O substitution on another O(2) atom. As it turns out, this asymmetric response has very little effect on $\theta_{a-atoms}$. It also has little effect on the K_{eq} of multiply substituted isotopologues in carbonate minerals, which is the main focus of the Schauble et al. (2006) study. A re-calculation of $K_{eq}[3866]$ in calcite using a grid with two distinct wave vectors from the present test models indicates that the asymmetry effect might be responsible for an up to 8×10^{-6} (i.e., 8 per meg) deviation for a particular C–O bond from the average over all bonds at 25°C, and the failure to account for this effect may be responsible for most of the difference in the K_{eq} values calculated with 2 wave-vector vs. 5 wave-vector grids in that study (Table 9). In fact, the re-calculated result using a 2 wave-vector sample of phonon frequencies from this study, combined with the frequency scale factor of 1.0331 from Schauble et al. (2006) and averaging over all 6 C–O bonds in the primitive calcite unit cell, yields a K_{eq} that is within 1 per meg of the Schauble et al. (2006) 5 wave-vector sample result, despite being based on models constructed using different pseudopotentials, electronic wave vector grids, and cutoff energies. This asymmetric substitution effect is smaller than other likely sources of error considered in the Schauble et al. (2006) study (such as anharmonicity and uncertainty in the frequency scale factor), and it does not change any of the significant conclusions reached in that work.

Comparison with previous determinations of $^{18}O/^{16}O$ fractionation. Although the present work is primarily concerned with the estimation of the mass dependence of oxygen isotope fractionation q_{a-b}, comparisons with measured or previously estimated $^{18}O/^{16}O$ fractionation factors are important for two reasons.

1. First-principles models that accurately reproduce $^{18}O/^{16}O$ fractionation factors can be reasonably be inferred to predict $^{17}O/^{16}O$ with similar accuracy, and thus yield realistic θ_{a-b}. They can also be inferred to predict $^{18}O/^{16}O$ fractionation factors for materials that have not yet been experimentally or empirically calibrated.

2. $^{18/16}\alpha_{a-b}$ is itself an important term in the conversion between $\theta_{a-atoms}$, $\theta_{b-atoms}$, θ_{a-b}, and $\Delta'^{17}O_{a-b}$.

Calibration of $^{18}O/^{16}O$ fractionation factors has been an ongoing project of stable isotope geochemistry for more than a half-century, and there is a large literature to provide a basis for comparisons. It is beyond the scope of the present chapter to provide a comprehensive evaluation of these calibrations, and excellent compilations are available in earlier volumes of this series, e.g., Chacko et al. (2001). However, it is worthwhile to examine a subset of materials spanning as much variability in crystal structure types and chemistries as is feasible.

Table 7. Comparison of reduced partition function ratios and exponents calculated with different density functionals, using frequency scale factors determined just for these six species. The PBE results are thus slightly different from the results listed above.

298.15 K	1000 ln$^{18/16}\beta$			$\theta_{\text{a–atoms}}$		
Substance	PBE	PBEsol	LDA	PBE	PBEsol	LDA
α-quartz	107.87	108.52	109.99	0.528129	0.528154	0.528176
Diaspore	89.91	91.42	93.59	0.529202	0.529158	0.529118
Anhydrite	96.40	98.27	100.20	0.528525	0.528487	0.528457
Calcite	98.83	99.96	101.67	0.528623	0.528604	0.528584
H_2O vapor	64.45	63.57	62.73	0.530030	0.530033	0.530035
CO_2	114.84	113.89	114.07	0.527949	0.527951	0.527945
RMS Misfit vs. PBE:		*1.23*	*2.71*		*0.000027*	*0.000051*

Table 8. Comparison of reduced partition function ratios and exponents calculated with different phonon wave vector grids. The number of distinct phonon wave vectors for each species is given in parentheses.

298.15 K	1000 ln$^{18/16}\beta$		$\theta_{\text{a–atoms}}$	
Substance	Fine grid	Coarse grid	Fine grid	Coarse grid
α-quartz (4,2)	108.70	108.69	0.528118	0.528118
Diaspore (4,2)	90.65	90.65	0.529193	0.529193
Anhydrite (2,1)	97.16	97.32	0.528515	0.528511
Calcite (5,2)	99.75	99.59	0.528609	0.528614
Aragonite (2,1)	99.16	99.20	0.528592	0.528591
RMS Misfit		*0.10*		*0.000002*

Table 9. Comparison of calculated ^{13}C–^{18}O–^{16}O–^{16}O clumping equilibrium constants in calcite. Results are given using both the carbonate-specific 1.0331 frequency scale factor used in Schauble et al. (2006), and the general 1.043 scale factor from the present study.

	Average K_{eq}(3866) with a 2 q-point phonon grid				
	273.15 K	298.15 K	373.15 K	573.15 K	1273.15K
Schauble et al. (2006)	1.000482	1.000403	1.000241	1.000073	1.000004
Present Study (SF 1.0331)	1.000491	1.000411	1.000247	1.000075	1.000005
Present Study (SF 1.043)	1.000500	1.000419	1.000253	1.000078	1.000005
	Average K_{eq}(3866) with a 5 q-point phonon grid				
Schauble et al. (2006)	1.000490	1.000410	1.000247	1.000075	1.000005

Here we focus on species with experimental calibrations and (ideally) ongoing interest for stable isotope studies, including calcite, the silicates quartz, albite, anorthite, diopside, forsterite, and zircon, and the rare-earth element phosphate mineral monazite. These are examined in terms of $^{18/16}\alpha_{\text{quartz–}x}$, the fractionation relative to quartz. The sulfate minerals barite and gypsum, the phosphate mineral fluorapatite, and the carbonate minerals calcite and dolomite are compared with liquid water, using the liquid–vapor model of Rosenbaum (1997) and our anharmonicity-corrected model for H_2O vapor to estimate the properties of liquid H_2O. This procedure likely introduces some error—and is clearly no longer *ab initio*. However, the systematics of model crystal fractionations vs. liquid water will still depend on the accuracies of the crystal models relative to each other. These comparisons are shown in Figure 5.
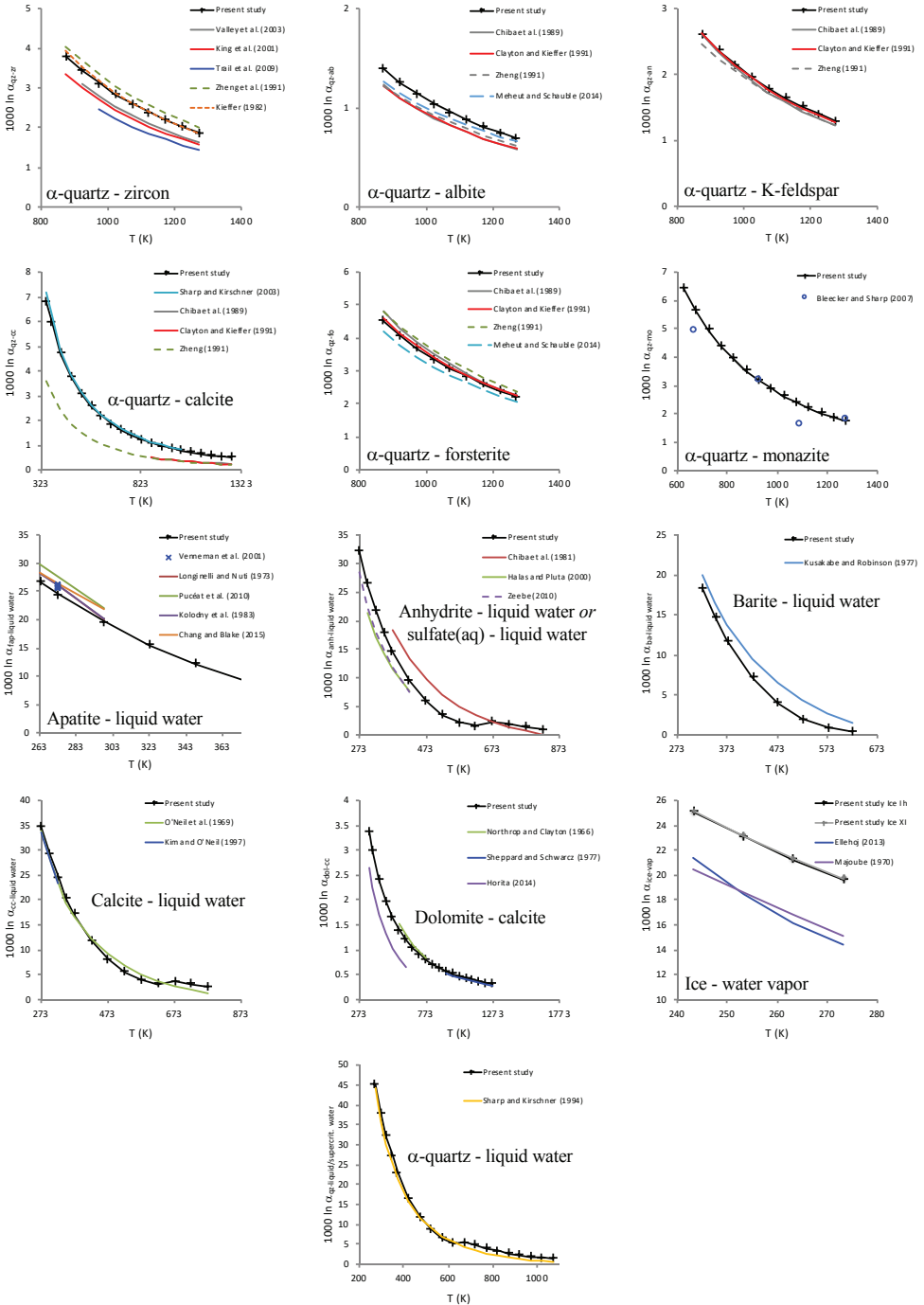
Figure 5. Comparison of calculated $^{18}O/^{16}O$ fractionation factors with previous experimental and theoretical studies. The models for anhydrite and fluorapatite are also compared with previous calibrations of the dissolved sulfate–water fractionation (Zeebe et al. 2010; Halas and Pluta 2000) and the dissolved phosphate–water fractionation (Chang and Blake 2015).

Experiments and empirical (field-based) calibrations of oxygen isotope fractionation between quartz and calcite give varying results—the empirical study of Sharp and Kirschner (1994) finds fractionation twice as large as a laboratory calibration (Clayton et al., 1989). The present models closely track the empirical calibration of Sharp and Kirschner (1994). It should be noted, however, that at least some other silicate–calcite fractionations show good agreement with direct exchange experiments, for instance phlogopite–calcite (-1.5‰ vs. -1.7‰ at 750 °C; Hu and Clayton 2003), and it should also be noted that the quartz–calcite fractionation predicted by Hayles et al. (2018) is intermediate between the Sharp and Kirschner (1994) and Clayton et al. (1989) calibrations. Fractionations among silicate minerals show reasonably good consistency with experimental and empirical calibrations, particularly for quartz–albite, quartz–anorthite, quartz–forsterite, and quartz–diopside, which all remain within 0.2–0.3‰ of tabulated experimental calibrations (Chiba et al. 1989, Clayton and Kieffer 1991) above 600 °C. Previous calibrations of the quartz–zircon fractionation are more variable, with theoretical estimates tending to predict larger fractionations than are observed. The present model behaves similarly, apparently overestimating the fractionation by 0.4–0.8‰ at 600 °C—and is in fact remarkably similar to a much earlier theoretical prediction of Kieffer (1982). Qualitatively, the present model is reasonable even for this mineral pair, but it is conceivable that a slightly higher frequency scale factor would be appropriate to consider for zircon, as suggested by both the overestimated quartz–zircon fractionation and the Raman and IR correlations for zircon. Quartz–monazite fractionations measured by Breecker and Sharp (2007) are in good agreement with the present models.

Mineral–water fractionations for phosphates, sulfates, and carbonates likewise generally show reasonable agreement with experiment, as has been found previously for similar types of models (e.g., Schauble et al. 2006; Meheut et al. 2007). The present models appear to underestimate sulfate–water and phosphate–water fractionations by up to 4‰ from 273–423 K. Interestingly, a model of meridianiite, $Mg(H_2O)_6 \cdot SO_4 \cdot 5H_2O$, which contains fully solvated SO_4^{2-} molecules, runs very close to previous calibrations of the aqueous sulfate–water fractionation (Halas and Pluta 2000; Zeebe 2010), falling within 1‰ of the both calibrations from 273–423 K. Our models closely match experimentally determined calcite–water and dolomite–water calibrations (e.g., O'Neil et al. 1969; Kim and O'Neil 1997; Horita 2014). The present results also match some previous dolomite–calcite fractionations well (e.g., Northrop and Clayton 1966; Sheppard and Schwarcz 1970) with greater disagreement with Horita (2014).

Calculated fractionations between water ice and vapor (using the harmonic vapor model) are considerably larger than measurements (e.g., Majoube 1970; Ellehoj et al. 2013), by ~5‰ at 273 K. Note that using anharmonically corrected values for vapor would worsen the mismatch (by ~3–4‰ at 273 K). The present estimates are in reasonable agreement with a previous model using similar DFT parameters, however (Meheut et al. 2007), suggesting that this is a systematic error for the theoretical method. This misfit may in part be consistent with the underestimation of lattice constants for ice crystals by the PBE functional, in that both suggest that the hydrogen bonding network of ice is not reproduced as accurately as other bond types. Relatively poor descriptions of hydrogen-bonding interactions in water vapor clusters, liquid water, and ice are a well-known defect of DFT methods (e.g., Gillan et al. 2016), and it should perhaps not be surprising that this is one case where the methods used in the present chapter are less accurate. In contrast, the estimated fractionation between liquid water (using the harmonic model of water vapor and the liquid–vapor fractionation from either Rosenbaum 1997 or Horita and Wesolowski 1994) and the water of hydration of gypsum is within 1‰ of experiments and empirical calibrations (Gazquez et al. 2017; Herwartz et al. 2017), with ~4‰ higher $^{18}O/^{16}O$ in hydration water at ~20 °C, and a temperature sensitivity of roughly -0.01‰/°C. This agrees with another recent theoretical result (Liu et al. 2019) using a similar type of model based on the PBEsol functional.

Comparison with previous determinations of θ_{a-b} ***and*** $\theta_{a-atoms}$***.*** Much less is known about equilibrium deviations from the canonical mass-fractionation relationship than about $^{18}O/^{16}O$ fractionation factors. In this section the available theoretical, experimental, and empirical calibration data are compared to our present results. In general, comparison of θ_{a-b} with experimental data depends on $\theta_{a-atoms}$, $\theta_{b-atoms}$, and $10^3 \ln^{18/16}\alpha_{a-b} = 10^3 \ln^{18/16}\beta_a - 10^3 \ln^{18/16}\beta_b$. The last term has just been discussed, with generally good agreement between model results and calibration, but suggesting some reason for concern that fractionations involving water will have modest systematic error. High-precision calibrations of θ have now been published for silica vs. liquid water, gypsum water vs. liquid water, and liquid water vs water vapor (Barkan and Luz 2005; Sharp et al. 2016; Gazquez et al. 2017; Herwartz et al. 2017). Theoretical calibrations for these and other systems have also been calculated recently by other authors (e.g., Cao and Liu 2011; Hayles et al. 2018). We compare these in turn (Fig. 6). In general, there is excellent agreement between the present results and those of Hayles et al. 2018, and reasonably good agreement with Cao and Liu (2011). This general agreement is consistent with the error analysis of Cao and Liu (2011), which demonstrated that theoretical estimates of $\theta_{a-atoms}$, in particular, are relatively robust even for simplified models.

The most extensive comparison sets come from Cao and Liu (2011) and Hayles et al. (2018). In the earlier work, $\theta_{a-atoms}$ (reported as κ, in their notation) is estimated for CO_2, CO, H_2O, and $H_6Si_2O_7$, as well as for gas-phase CO_3^{2-} and molecular clusters mimicking the structure of carbonate and silicate mineral structures. Cao and Liu (2011) mainly use hybrid density functional theory (B3LYP; Becke 1993) to estimate vibrational frequencies in their calculations. This method is closely related to the PBE functional used the present work—both are substantially based on gradient-corrected density functionals—but B3LYP incorporates a component of exact electron exchange. The exact exchange component of B3LYP is not as easily adapted to systems with periodic boundary conditions as pure density functionals such as PBE or BLYP, and so the calculations in Cao and Liu (2011) are limited to isolated atoms, molecules, and clusters, using atom-centered basis sets rather than the pseudopotential+plane wave basis set method applied here. However, a significant potential advantage for B3LYP is that it is typically observed to reproduce vibrational frequencies, molecular structures, and thermodynamic properties somewhat more accurately than PBE; for harmonic vibrational frequencies and zero point energies the scale factor for B3LYP is close to unity for typical molecular benchmark comparisons (e.g., Kesharwani et al. 2014; Alecu et al. 2010—updated at https://t1.chem.umn.edu/freqscale/index.html), and no scale factor is applied by Cao and Liu (2011) to their model calculations. However, the residual misfit after scaling, compared to harmonic frequencies inferred from spectroscopic measurements, is similar for both methods (e.g., Kesharwani et al. 2014). So cross-comparing results between the two studies is likely to give useful information about the reliability of both methods. Typical mismatches are ~5×10^{-5} or less for the small gas-phase molecules CO, CO_2, and H_2O, with somewhat larger mismatch of up to 2×10^{-4} for the bridging oxygen in vapor-phase disilicic acid $H_6Si_2O_7$, and similar disagreements between calcite with $CO_3^{2-}(v)$, and anorthite with $H_6SiAlO_7^-$. The relatively large mismatch between the present calcite model and the "calcite" result from Cao and Liu (2011) comes mainly from their proposed crystal–vapor correction to the gas-phase carbonate model. The close overall correspondence suggests that both model approaches are sufficiently accurate to be useful. The good match between molecules and crystals with similar bonding configurations around oxygen also suggests that a "building block" approach analogous to the methods developed for predicting $^{18}O/^{16}O$ fractionation by e.g. Garlick (1966) and Zheng (1991) will be even more well suited to predicting or rationalizing the mass dependence exponents, so that signatures in complex, incompletely characterized, and amorphous materials can likely be anticipated on the basis of simpler, better studied crystals and molecules.
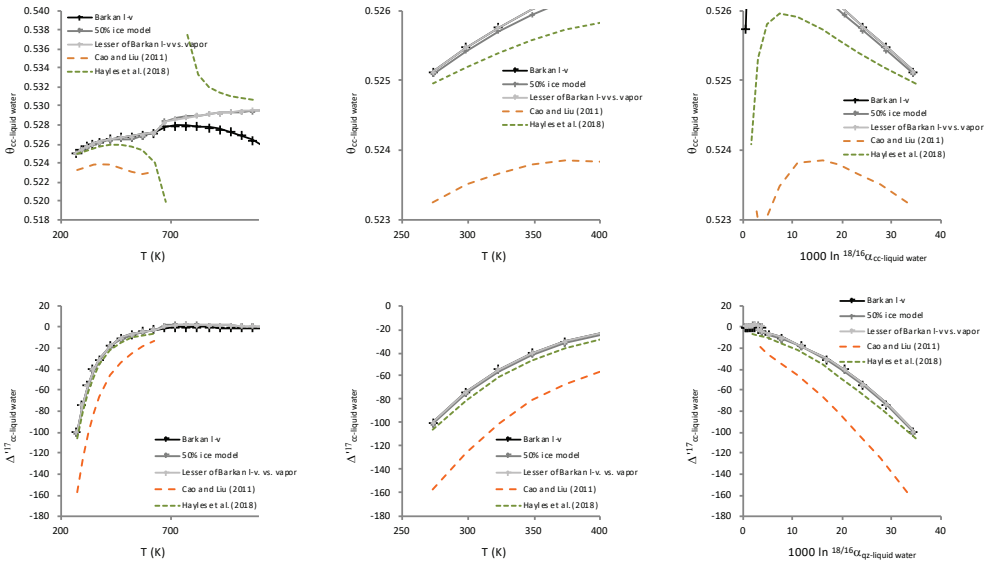
a. α-quartz – liquid water
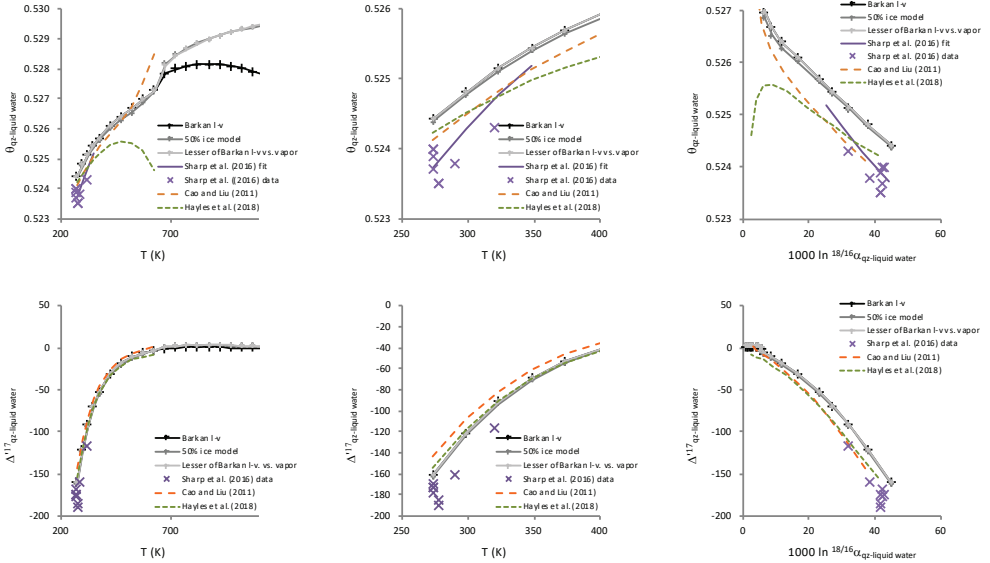
b. Calcite– liquid water

Figure 6. Comparison of calculated θ_{a-b} and $\Delta'^{17}O$ with previous experimental and theoretical studies in the quartz–water **(a)** and calcite–water **(b)** systems. For each system, the first row of three panels shows the exponent as a function of temperature over a wide and narrow (low) range, and also a function of the equilibrium $^{18}O/^{16}O$ fractionation. The irregular (hyperbolic) behavior of $\theta_{calcite–liquid}$ water at ~700 K reflects a change in sign of the calcite–water fractionation factor. Three variant models for $\theta_{liquid\ water–atoms}$ from the present study are used, based on either $\theta_{liquid\ water–water\ vapor}=0.529$ (Barkan l–v; Barkan and Luz 2005), the average of $\theta_{water\ vapor–atoms}$ and $\theta_{ice-Ih–atoms}$ (50% ice model), or the lesser of $\theta_{water\ vapor–atoms}$ and the Barkan l–v exponent. Calibration references: Sharp et al. (2016), Cao and Liu (2011), and Hayles et al. (2018). The y-axis units are per meg.

Hayles et al. (2018) focus on crystals and liquid water, mainly using a cluster-based method and hybrid density functional theory to estimate $^{18}O/^{16}O$ fractionation factors and $\theta_{a-atoms}$. Many of the same crystals are modeled here, and in general the agreement is remarkably good, with a deviation in $\theta_{quartz-atoms}$ of about 1×10^{-4} (at 273–373 K, then converging at higher temperatures), and deviations $< 2 \times 10^{-5}$ for $\theta_{calcite-atoms}$, $\theta_{dolomite-atoms}$, $\theta_{fluorapatite-atoms}$, and $\theta_{H_2O\ vapor-atoms}$ at 273 K and above. Calculated $^{18}O/^{16}O$ fractionations also generally agree, with the largest differences found for calcite and quartz at low temperatures. The present models predict ~1–1.5‰ higher $\ln^{18/16}\beta$ for α-quartz over the 273–373 K temperature range, and 1.5–2.8‰ lower $\ln^{18/16}\beta$ for calcite. Dolomite, fluorapatite, and water vapor models all agree within ~1‰ at temperatures ≥ 273 K. The overall magnitude of disagreement is similar to that observed between PBE and PBEsol-based models. There is at most a small systematic offset for the present PBE, periodic boundary condition models versus the Hayles et al. (2018) B3LYP, cluster models; the mean (signed) deviation in $\ln^{18/16}\beta$ for the set of quartz, calcite, dolomite, fluorapatite, and water vapor is 0.1‰ or less above 273 K.

The silica–water system has been studied empirically (Sharp et al. 2016), as well as with theoretical models, showing negative $\Delta'^{17}O$ in SiO_2 precipitates that is most pronounced in low temperature silica samples. All of the published theoretical models agree with the general trend of decreasing $\Delta'^{17}O_{SiO_2}$ and $\theta_{SiO_2-liquid\ water}$ in low temperature samples. In detail, the models appear to underestimate the deviation from the 0.528 exponent somewhat, particularly at the lowest temperatures, only reaching as low as $\theta_{SiO_2-liquid\ water} \approx 0.524$ vs. 0.523 and $\Delta'^{17}O_{SiO_2}$ ≈ -150 to -160 per meg vs. -180 to -190 per meg near 273 K. Note that the deviations in $\theta_{SiO_2-liquid\ water}$ at high temperatures in some models may be misleading, because they are highly sensitive to small changes in the $^{18}O/^{16}O$ fractionation factor and $\theta_{liquid\ water-atoms}$ that are difficult to resolve in measurements. The overall comparison suggests that these types of models will be useful guides to the behavior of $\Delta'^{17}O$ and $\theta_{mineral\ water}$ as a function of temperature, potentially even in low temperature samples where it is not obvious that exchange equilibrium is obtained.

The ^{17}O systematics of the water of hydration of gypsum has become a focus of interest in hydrological studies in arid climates. Gazquez et al. (2017) recommend $\theta_{gypsum\ water-parent\ brine}$ $= 0.5297 \pm 0.0012$. In a set of re-hydration experiments equilibrated at 21 ℃, Herwartz et al. (2017) find $\theta_{gypsum\ water-parent\ brine} = 0.5272 \pm 0.0019$, and they recommend a compromise value of 0.5286. Our models predict $\theta_{gypsum\ water-liquid\ water} \approx 0.528$ at 25 ℃, in good agreement with measurements. Our calculated $\theta_{gypsum\ water-liquid\ water}$ is consistently about 0.001 lower than the model calculations of Liu et al. (2019), though it is difficult to pinpoint the cause of the difference, and both results are consistent with measurements, given their uncertainties.

A system of great potential interest in future work is $CaCO_3$–liquid water, including both calcite and aragonite polymorphs of calcium carbonate. Although a number of measurements have been reported (e.g., Passey et al. 2014), it is difficult to convert these into a calibration vs. temperature. Initial results for calibration studies are beginning to appear in the literature (e.g., Wostbrock et al. in press; Voarintsoa et al. 2020; Bergel et al. 2020). The theoretical models of Hayles et al. (2018) and the present study are show excellent agreement; the adjusted, $CO_3^{2-}_{(v)}$-based model of Cao and Liu predicts lower $\theta_{carbonate-liquid\ water}$ than the other two models, but their unadjusted CO_3^{2-}-based model is closer to the more recent theoretical results. The overall trend vs. temperature in $\theta_{carbonate-liquid\ water}$ is similar in all models. The models are also generally in agreement with low $\Delta'^{17}O$ observed in carbonate minerals (e.g., Passey et al. 2014), and in reasonable agreement with the $\theta_{carbonate-liquid\ water}$ results of Wostbrock et al. (2020) (0.525–0.526 at 0 ℃ vs. 0.5251 in the present study, 0.5250 in Hayles et al. 2018, and 0.5253 in Guo and Zhou 2019). However, Voarinstsoa et al. (2020) and Bergel et al. (2020) measured a somewhat lower exponent ($\theta_{carbonate-liquid\ water} \approx 0.520$–0.523 at 283–308 K).

A final set of comparisons comes measurements of θ in higher-temperature systems, including tabulations aimed at finding a universally applicable mass fractionation exponent for silicate rocks (e.g., Rumble et al. 2007), including lunar samples (e.g., Young et al. 2016). As pointed out by Cao and Liu (2011), typical values in the range of 0.525–0.528 found in these compilations are broadly consistent with silicate–water fractionations at moderate–elevated temperatures, coinciding for instance with $\theta_{quartz–water}$ at temperatures from ~350–850 K. However, they are markedly at odds with the discovery of measurable $\Delta'^{17}O$ of several per meg in feldspars and quartz from high-temperature rocks, including lunar and terrestrial anorthosites (Young et al. 2016). The characteristically low $\Delta'^{17}O$ of feldspar-rich rocks, by ~10 per meg relative to related olivine and/or pyroxene-rich rocks, cannot be easily explained in the framework of the Urey (1947) harmonic oscillator theory of stable isotope fractionation, by nuclear field shift effects, or even by more exotic models such as the double-well potential.

Taken together, these comparisons indicate that theoretical models, even highly simplified ones, provide a useful guide to actual $^{18}O/^{16}O$ fractionations and θ, though direct testing is still limited to a few materials.

General properties of $\Delta'^{17}O$ in crystals relative to water vapor. Cao and Liu (2011), Dauphas and Schauble (2016), and Hayles et al. (2018) have shown that the variation in $\theta_{a–atoms}$ with changing chemical structure is highly systematic, moving below the high-temperature harmonic limit of ~0.5305 most strongly at low temperatures in materials with high force constants and relatively high-mass bond partners for oxygen. High force constants and relatively high-mass bond partners also correlate strongly with preferential incorporation of oxygen with high $^{18}O/^{16}O$, so it is not surprising to find correlation between $^{18}O/^{16}O$ fractionation factors and deviations in $\Delta'^{17}O$ in systems approaching equilibrium. The present results are also consistent with these principles. For instance, the low mass of hydrogen means that the mass fractionation exponent $\theta_{water\ vapor–atoms}$ stays close to the high-temperature limit even at Earth surface conditions, and this property largely carries over to liquid water and ice, which will have 0–20 per meg higher $\Delta'^{17}O$ than vapor at temperatures from 243 K (−30 °C) up to the critical point. This observation is important because many of the most promising geochemical applications of high-precision $\Delta'^{17}O$ measurements are in mineral–water systems.

Theoretical studies (e.g., Cao and Liu 2011; Hayles et al. 2018; and the present work) also find that the range of $\Delta'^{17}O$ between different mineral/mineral and mineral/molecule pairs is predicted to decrease quickly at equilibrium as temperature increases towards hydrothermal, metamorphic, and igneous conditions. However, the choice of reference exponent becomes relatively important at elevated temperatures. At 773 K (500 °C), the largest inter-phase $\Delta'^{17}O$ will be less than 10 per meg (e.g., 9 per meg for the forsterite–water vapor pair), relative to a 0.528 reference exponent, but could be greater than 20 per meg if the high-temperature equilibrium limit exponent of 0.53052 is the reference (where CO is a fractionating phase). Using the 0.528 reference, the range only slightly decreases to ~8 per meg at 1273 K (1000 °C), but the range is less than 5 per meg at this temperature if the 0.53052 high-temperature limiting exponent is used instead.

To illustrate these systematic behaviors, we have plotted the difference in $\Delta'^{17}O$ vs. $10^3 \ln^{18/16}\alpha_{a–water\ vapor}$ for a sample of the crystal types studied. Although there is substantial scatter, the systematic correlation in behavior of these two fractionation properties is clear (Fig. 7). Within the silicate mineral class (and especially for anhydrous silicates), strong $^{18}O/^{16}O$ fractionation is strongly correlated with negative $\Delta'^{17}O$, becoming most pronounced in structures with the highest Si:O ratios, such as quartz and alkali feldspars. Interestingly, hydrous Mg–Si–O–H silicates follow a similar trend of $\Delta'^{17}O$ vs. α. Among the anhydrous silicates studied, high Si:O corresponds to higher polymerization, whereas among the hydrous silicates high Si:O corresponds to lower polymerization because of Al:Si substitution into tetrahedral sites and increased OH concentrations in sheet silicates. The similar predicted $\Delta'^{17}O$ of kaolinite and lizardite indicates that tetrahedrally coordinated cations in silicates mainly
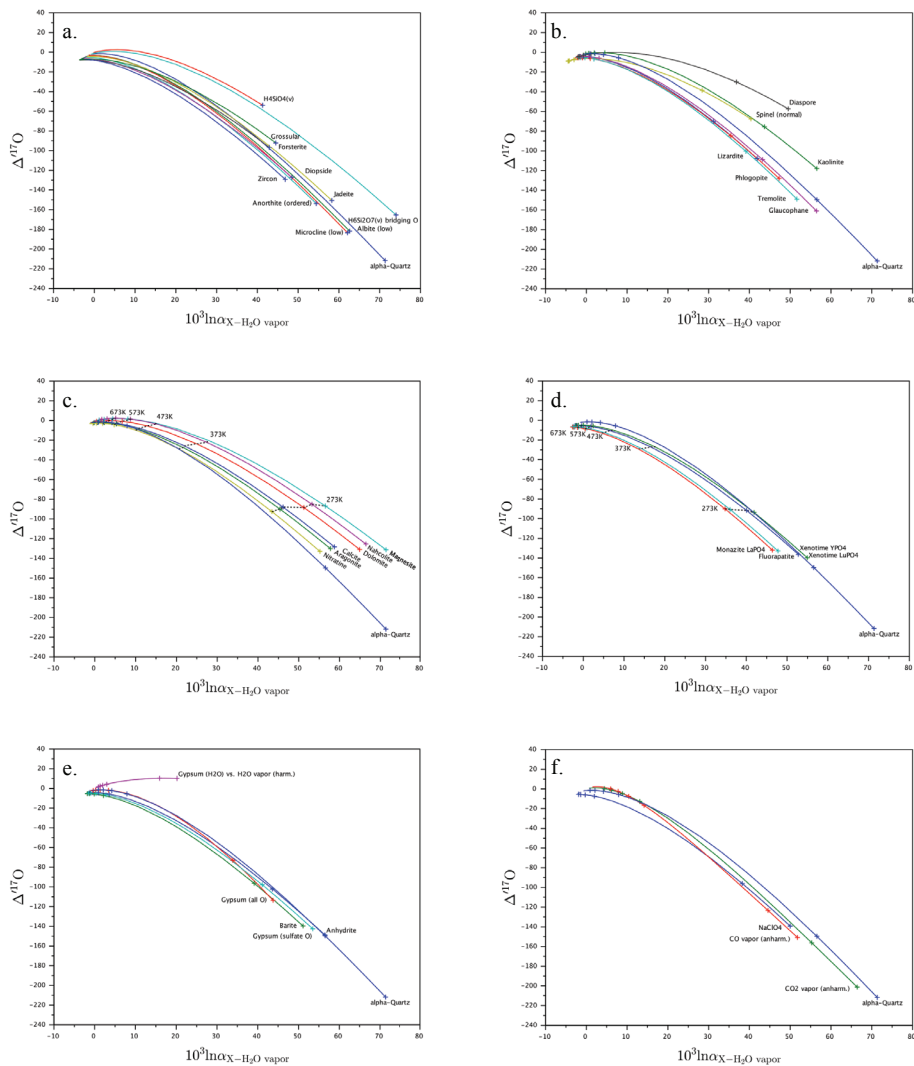
Figure 7. Calculated deviations of $\Delta'^{17}O$ from water vapor at equilibrium from 243–1573 K. **a)** anhydrous silicate minerals and molecules. **b)** hydrous silicate minerals, diaspore, and spinel. **c)** carbonates and nitratine. **d)** phosphates. **e)** sulfates. **f)** CO_2, CO, and sodium perchlorate. **g)** ice, liquid, and supercritical water. Unless otherwise specified, intermediate tick marks are given at 273 K, 373 K, 473 K, 573 K and 673 K on panels b–g. The same alpha-quartz data is shown in panels a–f, as a guide to the eye. The *y*-axis units are per meg.

control deviations from the reference fractionation exponent even though sites coordinated to octahedral Al^{3+} have a significantly higher affinity for ^{18}O (and ^{17}O) than sites coordinated to Mg^{2+}. Divalent metal carbonates show the importance of strong, low-coordination cation-oxygen bonds in controlling $\Delta'^{17}O$ even more strikingly, and it is possible to draw isothermal tie-lines at nearly constant $\Delta'^{17}O$ from aragonite and calcite through magnesite, spanning 10‰ in $^{18}O/^{16}O$ but only a few per meg in $\Delta'^{17}O$ at 273–373 K. In these crystals the strongest bonds are always internal to the carbonate group, and relative $^{18}O/^{16}O$ fractionation is controlled by weaker X^{2+}–O bonds characterized by low vibrational frequencies that do not affect the exponent as strongly. This behavior suggests that details of cation chemistry in

mixed-composition carbonates may not be very important for interpreting $\Delta'^{17}O$ signatures. Nitratine, with a different trigonal oxyanion (NO_3^-) and even weaker inter-molecular Na^+–O bonds, closely resembles its crystallographic cousin calcite. Phosphates show a similar near-invariance of $\Delta'^{17}O$ versus crystal chemistry, as do sulfates (excepting the water of hydration of gypsum). Silicate, phosphate, sulfate, and perchlorate crystals with the $ZTetO_4$ structural formula, including zircon, monazite, xenotime, barite, anhydrite, and $NaClO_4$, all show similar $\Delta'^{17}O$ vs. water vapor at a given temperature, relative to the 0.528 reference line, echoing the similarity noted above for $ZTriO_3$ carbonate and nitrate minerals. $\Delta'^{17}O$ vs. $^{18}O/^{16}O$ fractionation relationships for silicates, sulfates, phosphates, carbonates, nitrates, and perchlorates relative to liquid (or supercritical) water and water vapor follow a characteristically concave-down trajectory as temperature decreases. This characteristic relationship suggests that $\Delta'^{17}O$ relative to water could be crudely predicted even for crystals that have not be explicitly modeled, via comparison to other minerals of similar type. For silicates, in cases where $\ln^{18/16}\alpha_{mineral-water}$ can be reasonably well constrained, simply applying the $\Delta'^{17}O$ vs $^{18/16}\alpha_{quartz-water}$ relationship may be sufficient to give a useful approximation to the actual system of interest.

There is no indication that the apparent ~10 per meg deviations between different silicate phases found in lunar and terrestrial igneous rocks can be explained by equilibrium inter-mineral fractionation (Fig. 8). As an illustration, we compare the results obtained here with the high-temperature rock data in Figure 1. While the trend of lower $\Delta'^{17}O$ for quartz and feldspar relative to olivine and spinel is common to the data and the calculations, the magnitudes are entirely different. The calculations predict quartz and feldspar ~1 to 3 per meg lower in $\Delta'^{17}O$ than olivine, at most, at magmatic temperatures while the data exhibit differences ten times larger.
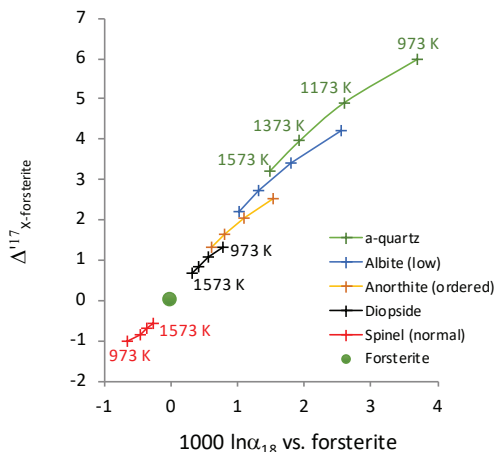

Figure 8. Calculated deviations of $\Delta'^{17}O$ in quartz, albite, anorthite, diopside and spinel relative to forsterite (Mg_2SiO_4) at equilibrium at temperatures from 973.15 K (700 °C) to 1573.15 K (1300 °C), plotted against each mineral's equilibrium $^{18}O/^{16}O$ fractionation relative to forsterite. The *y*-axis units are per meg.

SUMMARY

$\ln^{18/16}\beta$ and θ (and by extension $\Delta'^{17}O$ relationships at equilibrium) have been estimated for a variety of silicate, phosphate, sulfate, and carbonate minerals, as well as for representative nitrate, perchlorate, oxide, hydroxide, and ice crystals using first-principles electronic structure models. The results are generally in good agreement with previous studies of fractionation factors and mass-fractionation exponents, including both theoretical work and measurements. The nuclear volume component of the field shift effect is shown have a minor

or insignificant influence on fractionation and θ. A reconnaissance exploration of fractionation in an anharmonic, double-well potential does not find evidence for the generation of large $\Delta'^{17}O$ effects, at least for the most chemically plausible potential shapes. None of the results provide a convincing explanation for ~10 per meg $\Delta'^{17}O$ signatures observed in polymerized silicates in high-temperature terrestrial and lunar rock samples.

REFERENCES

Alecu IM, Zheng J, Zhao Y, Truhlar DG (2010) Computational thermochemistry: scale factor databases, scale factors for vibrational frequencies obtained from electronic model chemistries. J Chem Theory Comput 6:2872–2887. Note that the database generated for this reference has been subsequently updated (https://t1.chem.umn.edu/freqscale/index.html), although the updates do not affect the conclusions of the present work

Aliatis I, Lambruschi E, Mantovani L, Bersani D, Andò S, Diego Gatta G, Gentile P, Salvioli-Mariani E, Prencipe M, Tribaudino M, Lottici PP (2015) A comparison between ab initio calculated, measured Raman spectrum of triclinic albite (NaAlSi$_3$O$_8$). J Raman Spectrosc 46:501–508

Allan DR, Angel RJ (1997) A high-pressure structural study of microcline (KAlSi$_3$O$_8$) to 7 GPa. Eur J Mineral 9:263–275

Angeli I, Marinova KP (2013) Table of experimental nuclear ground state charge radii: An update. At Data Nucl Data Tables 99:69–95

Bao H, Cao X, Hayles JA (2015) The confines of triple oxygen isotope exponents in elemental and complex mass-dependent processes. Geochim Cosmochim Acta 170:39–50

Barkan E, Luz B (2005) High precision measurements of $^{17}O/^{16}O$ and $^{18}O/^{16}O$ ratios in H$_2$O. Rapid Commun Mass Spectrom 19:3737–42

Barone V (2005) Anharmonic vibrational properties by a fully automated second-order perturbative approach. J Chem Phys 122:014108

Becke AD (1993) Density-functional thermochemistry: III. The role of exact exchange. J Chem Phys 98:5648–5652

Begun GM, Beall GW, Boatner LA, Gregor WJ (1981) Raman spectra of rare earth orthophosphates. J Raman Spectrosc 11:273–278

Benedict WS, Gailar N, Plyler E K (1956) Rotation–vibration spectra of deuterated water vapor. J Chem Phys 24:1139–1165

Berenblut BJ, Dawson P, Wilkinson GR (1973) A comparison of the Raman spectra of anhydrite (CaSO$_4$), gypsum (CaSO$_4$.2H$_2$O). Spectrochim Acta 29A:29–36

Bergel SJ, Barkan E, Stein M, Affek HP (2020) Carbonate $^{17}O_{excess}$ as a paleo-hydrology proxy: Triple oxygen isotope fractionation between H$_2$O and biogenic aragonite, derived from freshwater mollusks. Geochim Cosmochim Acta 275:36–47

Bergquist BA, Blum JD (2007) Mass-dependent and -independent fractionation of Hg isotopes by photoreduction in aquatic systems. Science 318:417–420

Bertoluzza A, Monti P, Morelli MA, Battaglia MA (1981) A Raman and infrared spectroscopic study of compounds characterized by strong hydrogen-bonds J Mol Struct 73:19–29

Bigeleisen J (1996) Nuclear size and shape effects in chemical reactions. Isotope chemistry of the heavy elements. J Am Chem Soc 118:3676–3680

Bigeleisen J, Mayer MG (1947) Calculation of equilibrium constants for isotopic exchange reactions. J Chem Phys 15:261–267

Bish DL (1993) Rietveld refinement of the kaolinite structure at 1.5 K. Clays and Clay Minerals 41:738–744

Born M, Oppenheimer JR (1927) Zur Quantentheorie der Molekeln [translated: On the quantum theory of molecules] Ann Phys 389:457–484

Born K, Huang K (1956) Dynamical Theory of Crystal Lattices. Oxford University, New York

Bostrom D (1987) Single-crystal X-ray diffraction studies of synthetic Ni–Mg olivine solid solutions. Am Mineral 72:965–972

Breecker DO, Sharp ZD (2007) A monazite oxygen isotope thermometer. Am Mineral 1561–1572

Brehat F, Wyncke B (1985) Analysis of the temperature-dependent infrared active lattice modes in the ordered phase of sodium nitrate. J Phys C: Solid St Phys 18:4247–4259

Bunker PR (1970) The effect of the breakdown of the Born–Oppenheimer approximation on the determination of B$_e$ and w$_e$ for a diatomic molecule. J Mol Spectrosc 35:306–313

Busing W, Levy H (1958) A single crystal neutron diffraction study of diaspore, AlO(OH). Acta Crystallogr 11:798–803

Cano EJ, Sharp ZD, Shearer C K (2020) Distinct oxygen isotope compositions of the Earth and Moon. Nat Geosci 13:270–274

Cao X, Liu Y (2011) Equilibrium mass-dependent fractionation relationships for triple oxygen isotopes. Geochim Cosmochim Acta 75:7435–7445

Cao X, Bao H, Gao C, Liu Y, Huang F, Peng Y, Zhang Y (2019) Triple oxygen isotope constraints on the origin of ocean island basalts. Acta Geochim 38:327–334

Carteret C, De La Pierre M, Dossot M, Pascale F, Erba A, Dovesi R (2013) The vibrational spectrum of $CaCO_3$ aragonite: A combined experimental and quantum-mechanical investigation. J Chem Phys 138:014201

Castex J, Madon M (1995) Test of the vibrational modelling for the λ-type transitions: Application to the α–β quartz transition. Phys Chem Miner 22:1–10

Catti M, Ferraris G, Hull S, Pavese A (1995) Static compression, H disorder in brucite, Mg(OH)2, to 11 GPa: a powder neutron diffraction study. Phys Chem Miner 22:200–206

Chacko T, Cole DR, Horita J (2001) Equilibrium oxygen, hydrogen and carbon isotope fractionation factors applicable to geologic systems. Rev Mineral Geochem 43:1–81

Chang SJ, Blake RE (2015) Precise calibration of equilibrium oxygen isotope fractionations between dissolved phosphate and water from 3 to 37°C. Geochim Cosmochim Acta 150:314–329

Chaplot SL, Pintschovius L, Choudhury N, Mittal R (2006) Phonon dispersion relations, phase transitions, and thermodynamic properties of $ZrSiO_4$: Inelastic neutron scattering experiments, shell model, and first-principles calculations. Phys Rev B 73:094308

Chiba H, Kusakabe M, Hirano S-I, Matsuo S, Somiya S (1981) Oxygen isotope fractionation factors between anhydrite and water from 100 °C to 550 °C. Earth Planet Sci Lett 53:55–62

Chiba H, Chacko T, Clayton RN, Goldsmith JR (1989) Oxygen isotope fractionations involving diopside, forsterite, magnetite, and calcite: application to geothermometry. Geochim Cosmochim Acta 53:2985–2995

Chopelas A, Hofmeister AM (1991) Vibrational spectroscopy of aluminate spinels at 1 atm and of $MgAl_2O_4$ to over 200kbar. Phys Chem Miner 18:279–293

Clayton RN, Kieffer SW (1991) Oxygen isotopic thermometer calibrations. *In:* Stable Isotope Geochemistry: A Tribute to Samuel Epstein (eds. H.P. Taylor Jr. et al.). Geochem Soc Spec Publ vol. 3, p 3–10

Clayton RN, Grossman L, Mayeda T K (1973) A Component of Primitive Nuclear Composition in Carbonaceous Meteorites. Science 182:485–488

Clayton RN, Goldsmith JR, Mayeda T K (1989) Oxygen isotope fractionation in quartz, albite anorthite and calcite. Geochim Cosmochim Acta 53:725–733

Comodi P, Mellini M, Ungaretti L, Zanazzi PF (1991) Compressibility and high pressure structure refinement of tremolite, pargasite and glaucophane. Eur J Mineral 3:485–499

Comodi P, Liu Y, Zanazzi P F, Montagnoli M (2001) Structural and vibrational behaviour of fluorapatite with pressure. Part 1: in situ single-crystal X-ray diffraction investigation. Phys Chem Miner 28:219–224

Comodi P, Nazzareni S, Zanazzi PF, Speziale S (2008) High-pressure behavior of gypsum: A single-crystal X-ray study. Am Mineral 93:1530–1537

Császár AG, Czakó G, Furtenbacher T, Tennyson J, Szalay V, Shirin SV, Zobov NF, Polyansky OL (2005) Water vapor: On equilibrium structures of the water molecule. J Chem Phys 122:214305

Dal Corso A (2014) Pseudopotentials periodic table: From H to Pu. Comput Mater Sci 95:337–350

Dauphas N, Schauble EA (2016) Mass fractionation laws, mass-independent effects, and isotopic anomalies. Annu Rev Earth Planet Sci 44:709–783

Dawson P, Hargreave MM, Wilkinson GR (1977) Polarized i.r. reflection, absorption and laser Raman studies on a single crystal of $BaSO_4$. Spectrochim Acta 33A:83–93

de Villiers JPR (1971) Crystal structures of aragonite, strontianite, and witherite. Am Mineral 56:758–767

Deines P (2003) A note on intra-elemental isotope effects and the interpretation of non-mass-dependent isotope variations. Chem Geol 199:179–182

Dove MT, Heine V, Hammonds KD (1995) Rigid unit modes in framework silicates. Mineral Mag 59:629–639

Dunning TH Jr. (1989) Gaussian basis sets for use in correlated molecular calculations. I. The atoms boron through neon and hydrogen. J Chem Phys 90:1007–1023

Dupuis R, Benoit M, Tuckerman ME, Méheut M (2017) Importance of a fully anharmonic treatment of equilibrium isotope fractionation properties of dissolved ionic species as evidenced by Li^+(aq). Acc Chem Res 50:1597–1605

Earl BL (2008) The harmonic oscillator with a gaussian perturbation: evaluation of the integrals and example applications. J Chem Educ 85:453–457

Eckhardt R, Eggers D, Slutsky LJ (1970) Infrared spectrum of $NaNO_3$-I. Longitudinal and transverse internal modes. Spectrochim Acta 26A:2033–2049

Elcombe MM, Hulston JR (1975) Calculation of sulphur isotope fractionation between sphalerite and galena using lattice dynamics. Earth Planet Sci Lett 28:172–180

Ellehoj MD, Steen-Larsen HC, Johnsen SJ, Madsen MB (2013) Ice–vapor equilibrium fractionation factor of hydrogen and oxygen isotopes: Experimental investigations and implications for stable water isotope studies. Rapid Commun Mass Spectrom 27:2149–2158

Farquhar J, Bao H, Thiemens M (2000) Atmospheric influence of Earth's earliest sulfur cycle. Science 289:756–758

Farquhar J, Johnston DT, Wing BA, Habicht KS, Canfield DE, Airieau S, Thiemens MH (2003) Multiple sulphur isotopic interpretations of biosynthetic pathways: implications for biological signatures in the sulphur isotope record. Geobiology 1:27–36

Frisch MJ, Trucks GW, Schlegel HB, Scuseria GE, Robb MA, Cheeseman JR, Scalmani G, Barone V, Mennucci B, Petersson GA, Nakatsuji H, Caricato M, Li X, Hratchian HP, Izmaylov AF, Bloino J, Zheng G, Sonnenberg JL, Hada M, Ehara M, Toyota K, Fukuda R, Hasegawa J, Ishida M, Nakajima T, Honda Y, Kitao O, Nakai H, Vreven T, Montgomery JA Jr, Peralta JE, Ogliaro F, Bearpark M, Heyd JJ, Brothers E, Kudin KN, Staroverov VN, Keith T, Kobayashi R, Normand J, Raghavachari K, Rendell A, Burant JC, Iyengar SS, Tomasi J, Cossi M, Rega N, Millam JM, Klene M, Knox JE, Cross JB, Bakken V, Adamo C, Jaramillo J, Gomperts R, Stratmann RE, Yazyev O, Austin AJ, Cammi R, Pomelli C, Ochterski JW, Martin RL, Morokuma K, Zakrzewski VG, Voth GA, Salvador P, Dannenberg JJ, Dapprich S, Daniels AD, Farkas O, Foresman JB, Ortiz JV, Cioslowski J, Fox DJ (2013) Gaussian 09, Revision D.0,1 Gaussian, Inc., Wallingford CT

Fujii T, Moynier F, Albarède F (2009) The nuclear field shift effect in chemical exchange reactions. Chem Geol 267:139–156

Garlick GD (1966) Oxygen isotope fractionation in igneous rocks. Earth Planet Sci Lett 1:361–368

Garrity KF, Bennett JW, Rabe KM, Vanderbilt D (2014) Pseudopotentials for high-throughput DFT calculations. Comput Mater Sci 81:446–452

Gázquez F, Evans NP, Hodell DA (2017) Precise, accurate isotope fractionation factors ($\alpha^{17}O$ $\alpha^{18}O$, αD) for water and $CaSO_4 \cdot 2H_2O$ (gypsum). Geochim Cosmochim Acta 198:259–270

Geisler T, Popa K, Konings RJM (2016) Evidence for lattice strain, non-ideal behavior in the $(La_{1-x}Eu_x)PO_4$. Solid solution from X-ray diffraction and vibrational spectroscopy. Front Earth Sci 4:1–12

Giannozzi P, Baroni S, Bonini N, Calandra M, Car R, Cavazzoni C, Ceresoli D, Chiarotti GL, Cococcioni M, Dabo I, Dal Corso A, Fabris S, Fratesi G, de Gironcoli S, Gebauer R, Gerstmann U, Gougoussis C, Kokalj A, Lazzeri M, Martin-Samos L, Marzari N, Mauri F, Mazzarello R, Paolini S, Pasquarello A, Paulatto L, Sbraccia C, Scandolo S, Sclauzero G, Seitsonen AP, Smogunov A, Umari P, Wentzcovitch RM (2009) QUANTUM ESPRESSO: a modular and open-source software project for quantum simu- lations of materials. J Phys: Condens Matter 21:395502

Giarola M, Sanson A, Rahman A, Mariotto G (2011) Vibrational dynamics of YPO_4 and $ScPO_4$ single crystals: An integrated study by polarized Raman spectroscopy and first-principles calculations. Phys Rev B 83:224302

Gillan MG, Alfé D, Michaelides (2016) Perspective: How good is DFT for water? J Chem Phys 144:130901

Gillet P, Biellmann C, Reynard B, McMillan PF (1993) Raman spectroscopic studies of carbonates. Part I: High-pressure and high-temperature behaviour of calcite, magnesite, dolomite, and aragonite. Phys Chem Miner 20:1–18

Graf DL (1961) Crystallographic tables for the rhombohedral carbonates. Am Mineral 46:1283–1316

Gregorkiewitz M, Lebech B, Mellini M, Viti C (1996) Hydrogen positions and thermal expansion in lizardite-1T from Elba: A low-temperature study using Rietveld refinement of neutron diffraction data. Am Mineral 81:1111–1116

Grilly ER (1951) The vapor pressures of hydrogen, deuterium and tritium up to three atmospheres. J Am Chem Soc 73:843–846

Guo (2020) Kinetic clumped isotope fractionation in the $DIC–H_2O–CO_2$ system: Patterns, controls, and implications. Geochim Cosmochim Acta 268:230–257

Guo W, Zhou C (2019) Triple oxygen isotope fractionation in the $DIC–H_2O–CO_2$ system: A numerical framework and its implications. Geochim Cosmochim Acta 246:541–564

Halas P (2000) Empirical calibration of isotope thermometer $\delta^{18}O$ (SO_4^{2-})-$\delta^{18}O$ (H_2O) for low temperature brines. V Isotope Workshop. European Society for Isotope Research, Kraków, Poland, pp. 68–71

Hawthorne FC, Ferguson RB (1975) Anhydrous sulphates. II. Refinement of the crystal structure of anhydrite. Can Mineral 13:289–292

Hayles J, Gao C, Cao X, Liu Y, Bao H (2018) Theoretical calibration of the triple oxygen isotope thermometer. Geochim Cosmochim Acta 235:237–245

Hazen RM, Finger LW (1979) Crystal structure and compressibility of zircon at high pressure. Am Mineral 64:196–201

Hazen RM, Finger LW, Hemley RJ, Mao H K (1989) High-pressure crystal chemistry, amorphization of alpha-quartz. Solid State Commun 72 (1989) 507–511

Heidenreich JE, Thiemens MH (1986) A non-mass-dependent oxygen isotope effect in the production of ozone from molecular oxygen: The role of molecular symmetry in isotope chemistry. J Chem Phys 84:2129–2136

Hellwege KH, Lesch W, Plihal M, Schaack G (1970) Zwei-Phononen-Absorptionsspektren end dispersion der Schwingungszweige in Kristallen der Kalkspatstruktur (Translated title: "Two phonon absorption spectra and dispersion of phonon branches in crystals of calcite structure"). Z Phys 232:61–86

Herwartz D, Surma J, Voigt C, Assonov S, Staubwasser M (2017) Triple oxygen isotope systematics of structurally bonded water in gypsum. Geochim Cosmochim Acta 209:254–266

Herzberg, G (1966) Molecular Spectra and Molecular Structure III. Electronic Spectra and Electronic Structure of Polyatomic Molecules; Van Nostrand: New York. p 598

Hill RJ, Craig JR, Gibbs GV (1979) Systematics of the spinel structure type. Phys Chem Miner 4:317–319

Hill PS, Schauble EA, Tripati A (2020) Theoretical constraints on the effects of added cations on clumped, oxygen, and carbon isotope signatures of dissolved inorganic carbon species and minerals. Geochim Cosmochim Acta 269:496–539

Hofmeister AM, Bowey JE (2006) Quantitative infrared spectra of hydro-silicates and related minerals. Monthly Notices of the Royal Astronomical Society 367:577–591

Holzwarth NAW, Tackett AR, Matthews GE (2001) A Projector Augmented Wave (PAW) code for electronic structure calculations, Part I: atompaw for generating atom-centered functions. Computer Phys Commun 135:329–347

Horita J (2014) Oxygen and carbon isotope fractionation in the system dolomite–water–CO_2 to elevated temperatures. Geochim Cosmochim Acta 129:111–124

Horita J, Wesolowski DJ (1994) Liquid–vapor fractionation of oxygen and hydrogen isotopes of water from the freezing to the critical temperature. Geochim Cosmochim Acta 58:3425–3437

Hu G, Clayton RN (2003) Oxygen isotope salt effects at high pressure and high temperature and the calibration of oxygen isotope geothermometers. Geochim Cosmochim Acta 67:3227–3246

Hulston JR, Thode HG (1965) Variations in the S^{33}, S^{34}, and S^{36} contents of meteorites and their relation to chemical and nuclear effects, J Geophys Res 70:3475–3484

Iishi K (1979) Phonon spectroscopy and lattice dynamical calculations of anhydrite and gypsum. Phys Chem Miner 4:341–359

Jacobsen SD, Smyth JR, Swope RJ, Downs RT (1998) Rigid-body character of the SO_4 groups in celestine, anglesite and barite. Can Mineral 36:1053–1060

Jayasooriya UA, Kettle SFA, Mahasuverachai S, White RP (1996) Lattice vibrations in compounds crystallising with the baryte structure. J Chem Soc, Faraday Trans 92:3625–3628

Jensen HJA et al. (2015) DIRAC, a relativistic ab initio electronic structure program, Release DIRAC15 (see http://www.diracprogram.org)

Jollet F, Torrent M, Holzwarth N (2014) Generation of projector augmented-wave atomic data: A 71 element validated table in the XML format. Comput Phys Commun 185:1246–1254

Kendall RA, Dunning TH, Harrison RJ (1992) Electron affinities of the first-row atoms revisited. Systematic basis sets and wave functions. J Chem Phys 96:6976–6806

Kesharwani M K, Brauer B, Martin JML (2014) Frequency, zero-point vibrational energy scale factors for double-hybrid density functionals (and other selected methods): Can anharmonic force fields be avoided? J Phys Chem A 119:1701–1714

Kieffer SW (1982) Thermodynamics and lattice vibrations of minerals: 5. Applications to phase equilibria, isotopic fractionation, and high-pressure thermodynamic properties. Rev Geophys Space Phys 20:827–849

Kim S-T, O'Neil JR (1997) Equilibrium and nonequilibrium oxygen isotope effects in synthetic carbonates. Geochim Cosmochim Acta 61:3461–3475

King WH (1984) Isotope Shifts in Atomic Spectra (Physics of Atoms and Molecules). Plenum, New York

King EM, Valley JW, Davis DW, Kowallis BJ (2001) Empirical determination of oxygen isotope fractionation factors for titanite with respect to zircon and quartz. Geochim Cosmochim Acta 65:3165–3175

Kleinman LI, Wolfsberg M (1973) Corrections to the Born–Oppenheimer approximation and electronic effects on isotopic exchange equilibria. J Chem Phys. 59:2043–2053

Knight KS, Price GD (2008) Powder neutron-diffraction studies of clinopyroxenes. I. The crystal structure and thermoelastic properties of jadeite between 1.5 and 270 K. Can Mineral 46:1593–1622

Knyazev DA, Myasoedov NF (2001) Specific effects of heavy nuclei in chemical equilibrum. Sep Sci Technol 36:1677–1696

Kolesov BA, Geiger CA (2004) A Raman spectroscopic study of Fe-Mg olivines. Phys Chem Miner 31:142–154

Kolodny Y, Luz B, Navon O (1983) Oxygen isotope variations in phosphate of biogenic apatites. I. Fish bone apatite—rechecking the rules of the game. Earth Planet Sci Lett 64:398–404

Kusakabe M, Robinson BW (1977) Oxygen and sulfur isotope equilibria in the $BaSO_4$-HSO_4^--H_2O system from 110 to 350ºC and applications. Geochim Cosmochim Acta 41:1033–1040

Leadbetter AJ, Ward RC, Clark JW, Tucker PA, Matsuo T, Suga H (1985) Ice XI: The equilibrium low-temperature structure of ice. J Chem Phys 82:424

Lefebvre J, Currat R, Fouret R, More M (1980) Etude par diffusion neutronique des vibrations de reseau dans le nitrate de sodium. J Phys C: Solid Stat Phys. 13:4449–4461

Lejaeghere K et al. (2016) Reproducibility in density functional theory calculations of solids. Science 351:1394–1395

Leroy G, Leroy N, Penel G, Rey C, Lafforgue P, Bres E (2000) Polarized micro-Raman study of fluorapatite single crystals. Appl Spectrosc 54:1521–1527

Levin NE, Raub TD, Dauphas N, Eiler JM (2014) Triple oxygen isotope variations in sedimentary rocks. Geochim Cosmochim Acta 139:173–189

Lin C- K, Chang H-C, Lin SH (2007) Symmetric double-well potential model and its application to vibronic spectra: Studies of inversion modes of ammonia and nitrogen-vacancy defect centers in diamond. J Phys Chem A 111:9347–9354

Liu Q, Tossell JA, Liu Y (2010) On the proper use of the Bigeleisen–Mayer equation and corrections to it in the calculation of isotopic fractionation equilibrium constants. Geochim Cosmochim Acta 74:6965–6983

Liu T, Artacho E, Gázquez F, Walters G, Hodell D (2019) Prediction of equilibrium isotopic fractionation of the gypsum/bassanite/water system using first-principles calculations. Geochim Cosmochim Acta 244:1–11

Longinelli A, Nuti S (1973) Revised phosphate–water isotopic temperature scale. Earth Planet Sci Lett 19:373–376

Lutz HD, Becker RA, Kruska BG, Berthold HJ (1979) Raman-, IR- und FIR-Messungen an wasserfreiem Natriumperchlorat NaClO4 im Temperaturbereich zwischen 90 und 600 K. Spectrochim Acta 35A:797–806

Luz B, Barkan E (2010) Variations of $^{17}O/^{16}O$ and $^{18}O/^{16}O$ in meteoric waters. Geochim Cosmochim Acta 74:6276–86

Majoube M (1970) Fractionation factor of ^{18}O between water vapour and ice. Nature 226:1242

Mantz AW, Maillard JP (1975) Ground state molecular constants of $^{12}C^{16}O$, J Mol Spectrosc 57:155–159

Maschio L, Demichelis R, Orlando R, De La Pierre M, Mahmoud A, Dovesi R (2014) The Raman spectrum of grossular garnet: a quantum mechanical simulation of wavenumbers and intensities. J Raman Spectrosc 45:710–715

Matsuhisa Y, Goldsmith JR, Clayton RN (1978) Mechanisms of hydrothermal crystallization of quartz at 250°C and 15 kbar. Geochim Cosmochim Acta 42:173–182

Mauersberger K (1987) Ozone isotope measurements in the stratosphere. Geophys Res Lett 14:80–83

McKeegan KD, Kallio APA, Heber VS, Jarzebinski G, Mao PH, Coath CD, Kunihiro T, Wiens RC, Nordholt JE, Moses RW Jr., Reisenfeld DB, Jurewicz AJG, Burnett DS (2011) The oxygen isotopic composition of the sun inferred from captured solar wind. Science 332:1528–1532

Méheut M, Schauble EA (2014) Silicon isotope fractionation in silicate minerals: Insights from first-principles models of phyllosilicates, albite and pyrope. Geochim Cosmochim Acta 134:137–154

Méheut M, Lazzeri M, Balan E, Mauri F (2007) Equilibrium isotopic fractionation in the kaolinite, quartz, water system: prediction from first-principles density-functional theory. Geochim Cosmochim Acta 71:3170–3181

Merli M, Ungaretti L, Oberti R (2000) Leverage analysis and structure refinement of minerals. Am Mineral 85:532–542

Merrick JP, Moran D, Radom L (2007) An evaluation of harmonic vibrational frequency scale factors. J Phys Chem A 111:11683–11700

Miska H, Norum B, Hynes MV, Bertozzi W, Kowalski S, Rad FN, Sargent CP, Sasanuma T (1979) Precise measurement of the charge-distribution differences of the oxygen isotopes. Phys Lett B 83:165–168

Mittal R, Chaplot SL, Choudhury N, Loong C-K (2007) Inelastic neutron scattering, lattice dynamics and high-pressure phase stability in $LuPO_4$ and $YbPO_4$. J Phys Condens Matter 19:446202

Møller C, Plesset, MS (1934) Note on an Approximation Treatment for Many-Electron Systems. Phys Rev 46:618–622

Ni Y, Hughes JM, Mariano AN (1995) Crystal chemistry of the monazite and xenotime structures. Am Mineral 80:21–26

Nomura M, Higuchi N, Fujii Y (1996) Mass dependence of uranium isotope effects in the U(IV)–U(VI) exchange reaction. J Am Chem Soc 118:9127–9130

Northrop DA, Clayton RN (1966) Oxygen-isotope fractionation in systems containing dolomite. J Geol 74:174–196

O'Neil JR, Clayton RN, Mayeda T K (1969) Oxygen isotope fractionation in divalent metal carbonates. J Chem Phys 51:5547–5558

Pack A, Herwartz D (2014) The triple oxygen isotope composition of the Earth mantle and understanding $\delta^{17}O$ variations in terrestrial rocks and minerals. Earth Planet Sci Lett 390:138–45

Pack A, Tanaka R, Hering M, Sengupta S, Peters S, Nakamura E (2016) The oxygen isotope composition of San Carlos olivine on the VSMOW2-SLAP2 scale. Rapid Commun Mass Spectrom 30, 1495–1504

Passey BH, Hu H, Ji H, Montanari S, Li S, Henkes GA, Levin NE (2014) Triple oxygen isotopes in biogenic and sedimentary carbonates. Geochim Cosmochim Acta 141:1–25

Paul GL, Pryor AW (1972) The study of sodium nitrate by neutron diffraction. Acta Crystallographica B 28:2700–2702

Pavese A, Catti M, Price GD, Jackson RA (1992) Interatomic potentials for $CaCO_3$ polymorphs (calcite and aragonite), fitted to elastic and vibrational data. Phys Chem Miner 19:80–87

Perdew JP, Zunger A (1981) Self-interaction correction to density-functional approximations for many-electron systems. Phys Rev B 23:5048–5079

Perdew JP, Burke K, Ernzerhof M (1996) Generalized gradient approximation made simple. Phys Rev Lett 77:3865–3868

Perdew JP, Ruzsinszky A, Csonka GI, Vydrov OA, Scuseria GE, Constantin LA, Zhou X, Burke K (2007) Restoring the density-gradient expansion for exchange in solids and surfaces. Phys Rev Lett 100:136406

Pilati T, Demartin F, Gramaccioloi CM (1998) Lattice-dynamical estimation of atomic displacement parameters in carbonates: calcite, aragonite $CaCO_3$, dolomite $CaMg(CO_3)_2$ and magnesite $MgCO_3$. Acta Crystallogr B 54:515–523

Pinella C, Blanchard M, Balan E, Natarajan S K, Vuilleumier R, Mauri F (2015) Equilibrium magnesium isotope fractionation between aqueous Mg^{2+} and carbonate minerals: Insights from path integral molecular dynamics. Geochim. Cosmochim. Acta 163:126–139

Prandini G, Marrazzo A, Castelli IE, Mounet N, Marzari N (2018) Precision and efficiency in solid-state pseudopotential calculations. npj Comput Mater 4:72

Prencipe M, Mantovani L, Tribaudino M, Bersani D, Lottici PP (2012) The Raman spectrum of diopside: a comparison between ab initio calculated and experimentally measured frequencies. Eur J Mineral 24:457–464

Prencipe M, Maschio L, Kirtman B, Salustro S, Erba A, Dovesi R (2014) Raman spectrum of $NaAlSi_2O_6$ jadeite. A quantum mechanical simulation. J Raman Spectrosc 45:703–709

Pucéat E, Joachimski MM, Bouilloux A, Monna F, Bonin A, Motreuil S, Moriniere P, Hénard S, Mourin J, Dera G, Quesne D (2010) Revised phosphate–water fractionation equation reassessing paleotemperatures derived from biogenic apatite. Earth Planet Sci Lett 298:135–142

Redhammer GJ (1998) Mössbauer spectroscopy, Rietveld refinement on synthetic ferri-Tschermak's molecule $CaFe^{3+}(Fe^{3+}Si)O_6$ substituted diopside. Eur J Mineral 10:439–452

Richet P, Bottinga Y, Javoy M (1977) A review of hydrogen, carbon, nitrogen, oxygen, sulphur, and chlorine stable isotope fractionation among gaseous molecules. Annu Rev Earth Planet Sci 5:65–110

Rodehorst U, Geiger CA, Armbruster T (2002) The crystal structures of grossular, spessartine between 100 and 600 K and the crystal chemistry of grossular–spessartine solid solutions. Am Mineral 87 (2002) 542–549

Rosenbaum JM (1997) Gaseous, liquid, and supercritical fluid H_2O and CO_2: oxygen isotope fractionation behavior. Geochim Cosmochim Acta 61:4993–5003

Ross NL (1997) The equation of state and high-pressure behaviour of magnesite. Am Mineral 82:682–688

Ross NL, Reeder RJ (1992) High-pressure structural study of dolomite and ankerite. Am Mineral 77:412–421

Rumble D, Miller MF, Franchi IA, Greenwood RC (2007) Oxygen three-isotope fractionation lines in terrestrial silicate minerals: An inter-laboratory comparison of hydrothermal quartz and eclogitic garnet. Geochim Cosmochim Acta 71:3592–3600

Rutt HN, Nicola JH (1974) Raman spectra of carbonates of calcite structure. J Phys C 7:4522–4528

Sass RL, Scheuerman RF (1962) The crystal structure of sodium bicarbonate. Acta Crystallogr 15:77–81

Sato R K, McMillan PF (1987) An infrared and Raman study of the isotopic species of alpha-quartz. J Phys Chem 91:3494–3498

Schauble EA (2007) Role of nuclear volume in driving equilibrium stable isotope fractionation of mercury, thallium, and other very heavy elements. Geochim Cosmochim Acta 71:2170–2189

Schauble EA (2011) First-principles estimates of equilibrium magnesium isotope fractionation in silicate, oxide, carbonate, hexaaquamagnesium(2+) crystals. Geochim Cosmochim Acta 75:844–869

Schauble EA (2013) Modeling nuclear volume isotope effects in crystals. PNAS 110:17714–17719

Schauble EA, Rossman GR, Taylor HP Jr. (2003) Theoretical estimates of equilibrium chlorine-isotope fractionations. Geochim Cosmochim Acta 67:3267–3281

Schauble EA, Ghosh P, Eiler JM (2006) Preferential formation of ^{13}C–^{18}O bonds in carbonate minerals, estimated using first-principles lattice dynamics. Geochim Cosmochim Acta 70:2510–2529

Sharma BD (1965) Sodium bicarbonate and its hydrogen atom. Acta Crystallogr 18:818–819

Sharp ZD, Kirschner DL (1994) Quartz–calcite oxygen isotope thermometry: a calibration based on natural isotopic variations. Geochim Cosmochim Acta 58:4491–4501

Sharp ZD, Gibbons JA, Maltsev O, Atudorei V, Pack A, Sengupta S, Shock EL, Knauth LP (2016) A calibration of the triple oxygen isotope fractionation in the SiO_2–H_2O system and applications to natural samples. Geochim Cosmochim Acta 186:105–119

Sheppard SMF, Schwarcz HP (1970) Fractionation of carbon and oxygen isotopes and magnesium between coexisting metamorphic calcite and dolomite. Contrib Mineral Petrol 26:161–198

Singhal RP, Moreira JR, Caplan HS (1970) RMS charge radii of $^{16,17,18}O$ by elastic electron scattering. Phys Rev Lett 24:73–75

Smith JV, Artioli G (1986) Low albite, $NaAlSi_3O_8$: Neutron diffraction study of crystal structure at 13 K. Am Mineral 71:727–733

Syme RWG, Lockwood DJ, Kerr HJ (1977) Raman spectrum of synthetic zircon ($ZrSiO_4$), thorite ($ThSiO_4$). J Phys C: Solid State Phys 10:1335–1348

Tachikawa M, Shiga M (2005) Geometrical H/D isotope effect on hydrogen bonds in charged water clusters. J Am Chem Soc 127:11908–11909

Topsakal M, Wentzcovitch RM (2014) Accurate projected augmented wave (PAW) datasets for rare-earth elements (RE = La–Lu). Comput Mater Sci 95:263–270

Toupry-Krauzman N, Poulet H (1978) Temperature dependence of the Raman spectra of $NaClO_4$, in relation to the 581 K phase transition. J Raman Spectrosc 7:1–6

Trail D, Bindeman IN, Watson EB, Schmitt A K (2009). Experimental calibration of oxygen isotope fractionation between quartz and zircon. Geochim Cosmochim Acta 73:7110–7126

Urey HC (1947) The thermodynamic properties of isotopic substances. J Chem Soc (London) 562–581

Valley JW, Bindeman IN, Peck WH (2003). Empirical calibration of oxygen isotope fractionation in zircon. Geochim Cosmochim Acta 67:3257–3266

Venneman TW, Hegner E, Cliff G, Benz GW (2001) Isotopic composition of recent shark teeth as a proxy for environmental conditions. Geochim Cosmochim Acta 65:1583–1599

Voarintsoa NRG, Barkan E, Bergel S, Vieten R, Affek HP (2020) Triple oxygen isotope fractionation between $CaCO_3$ and H_2O in inorganically precipitated calcite and aragonite. Chem Geol 539:119500

Wainwright J, Starkey J (1971) A refinement of the structure of anorthite. Z Kristallogr 133:75–84

Wartchow R, Berthold HJ (1978) Refinement of the crystal structure of sodium perchlorate ($NaClO_4$). Z Krystallogr 147:307–17

Webb MA, Miller TF III (2014) Position-specific and clumped stable isotope studies: Comparison of the urey and path-integral approaches for carbon dioxide, nitrous oxide, methane, and propane. J Phys Chem A 118:467–474

Widanagamage IH, Schauble EA, Scher HD, Griffith EM (2014) Stable strontium isotope fractionation in synthetic barite. Geochim Cosmochim Acta 147:58–75

Wiechert U, Halliday AN, Lee D-C, Snyder GA, Taylor LA, Rumble D (2001) Oxygen Isotopes and the Moon-Forming Giant Impact. Science 294:345–348

Wostbrock JAG, Brand U, Coplen TB, Swart P K, Carlson SJ, Brearley A, Sharp ZD (2020) Calibration of carbonate–water triple oxygen isotope fractionation: seeing through diagenesis in ancient carbonates. Geochim Cosmochim Acta 288:369-388

Yagi K, Hirao K, Taketsugu T, Schmidt M, Gordon MS (2004) Ab initio vibrational state calculations with a quartic force field: applications to H_2CO, C_2H_4, CH_3OH, CH_3CCH, and C_6H_6. J Chem Phys 121:1383–1389

Yamamoto A, Utida T, Murata H (1976) Coulomb interactions and optically-active vibrations of ionic crystals–I. Theory and applications to NaNO$_3$. J Phys Chem Solids 37:693–698

Young ED, Galy A, Nagahara H (2002) Kinetic and equilibrium mass-dependent isotope fractionation laws in nature and their geochemical and cosmochemical significance. Geochim Cosmochim Acta 66:1095–1104

Young ED, Kohl IE, Warren PH, Rubie DC, Jacobson SA, Morbidelli A (2016) Oxygen isotopic evidence for vigorous mixing during the Moon-forming giant impact. Science 351:493–496

Zeebe RE (2010) A new value for the stable oxygen isotope fractionation between dissolved sulfate ion and water. Geochim Cosmochim Acta 74:818–828

Zhang M, Wruck B, Graeme Barber A, Salje E KH, Carpenter MA (1996) Phonon spectra of alkali feldspars: Phase transitions and solid solutions. Am Mineral 81:92–104

Zhang Y, Liu Y (2018) The theory of equilibrium isotope fractionations for gaseous molecules under super-cold conditions. Geochim Cosmochim Acta 238:123–149

Zheng Y-F (1991) Calculation of oxygen isotope fractionation in anhydrous silicate minerals. Geochim Cosmochim Acta 57:1079–1091

Zúñiga J, Bastida A, Alacid M, Requena A (2001) Variational calculations of rovibrational energies for CO$_2$. J Mol Spectrosc 205:62–72